

Original Article

Cite this article: He X, Fu C, Yan Z, Wang B, Niu M, and Li X (2021) Petrogenesis and tectonic implication of the lower Silurian high-Sr/Y subvolcanic rocks from the South Qilian suture zone in the Qilian Orogen, NW China. *Geological Magazine* 158: 1383–1402. <https://doi.org/10.1017/S0016756820001442>


Received: 23 August 2020
Revised: 6 December 2020
Accepted: 15 December 2020
First published online: 1 March 2021

Keywords:

early Silurian; subvolcanic rocks; thickened crust; post-collision; Lajishan; South Qilian suture

Author for correspondence: Changlei Fu,
Email: fucl815@126.com

Petrogenesis and tectonic implication of the lower Silurian high-Sr/Y subvolcanic rocks from the South Qilian suture zone in the Qilian Orogen, NW China

Xiaohu He¹, Changlei Fu^{2,3} , Zhen Yan², Bingzhang Wang³, Manlan Niu⁴ and Xiucai Li⁴

¹Department of Geology, School of Earth Sciences, Yunnan University, Kunming 650091, China; ²Institute of Geology, Chinese Academy of Geological Sciences, Beijing 100037, China; ³Key Laboratory of the Northern Qinghai–Tibet Plateau Geological Processes and Mineral Resources, Qinghai Geological Survey Institute, Xining 810012, China and ⁴Department of Resources and Environment, Hefei University of Technology, Hefei 230009, China

Abstract

As the remnant of the South Qilian Ocean, the South Qilian suture zone recorded abundant information on the Cambrian–Ordovician subduction history of the southern branch of the Proto-Tethyan Ocean. However, the closure timing of the South Qilian Ocean and subsequent collision are poorly constrained. In this study, we report early Silurian (433–435 Ma) U–Pb ages of felsic subvolcanic rocks from Lianhuashan, Ayishan and Shihuiyao of the Lajishan district within the South Qilian suture zone. They intruded the Late Ordovician – Silurian sedimentary or Late Ordovician volcanic rocks and have high SiO₂ (61.43–73.06 wt%), Sr/Y ratios with significant different rare earth elements (REEs) and trace-element spider diagrams, and Sr–Nd isotopic compositions, probably implying that they were formed through distinctly different generation mechanisms. Geochemistry of the Lianhuashan dacites reveals compositions typical of adakitic rocks derived from partial melting of lower crust in a thickened setting. The Ayishan dacites were derived from partial melting of crustal materials with the involvement of minor peridotite mantle, and the Shihuiyao rhyolites were derived from partial melting of felsic crust. The similar geochemical characteristics of coeval post-collisional igneous rocks in the Central Qilian and South Qilian blocks indicates that the lower Silurian subvolcanic rocks were generated in a thickened crust of post-collisional setting. Considering their intrusive contacts with Late Ordovician – Silurian retro-foreland basin and Late Ordovician collisional volcanic rocks, we propose that the South Qilian suture zone was at a transitional stage from collisional to post-collisional during the early Silurian Period.

1. Introduction

The Qilian Orogen is located on the northern margin of the Tibetan Plateau and adjacent areas, including the Qaidam Block to the south, the Tarim Block to the NW and the Alxa Block to the NE (Fig. 1a). It is a typical accretionary-collisional orogenic belt which connects with the eastern Qinling Orogen and SW Kunlun Orogen (Fig. 1a). It is considered to have developed as a result of the closure of the Proto-Tethyan Ocean and consists of two suture zones (the South Qilian suture to the south and the North Qilian suture to the north) sandwiched between the Alxa, Central Qilian and South Qilian blocks (Fig. 1b; Xiao *et al.* 2009; Gehrels *et al.* 2011; Yan *et al.* 2015; Zhang *et al.* 2015a; Xia *et al.* 2016; Fu *et al.* 2018a, 2019a; Li *et al.* 2018a; Zuza *et al.* 2018). To constrain the evolutionary history of the Qilian Orogen, previous researchers have investigated the ophiolite, island-arc, accretionary complex and igneous rocks associated with subduction, and collisional and post-collisional magmatism from geochronology, geochemistry and Sr–Nd–Hf isotopic compositions (Qian *et al.* 2001; Xiao *et al.* 2009; Tseng *et al.* 2009; Wu *et al.* 2010; Guo *et al.* 2015; Zhang *et al.* 2015b; Xia *et al.* 2016; Wang *et al.* 2017a; Fu *et al.* 2018c; Cui *et al.* 2019; Yan *et al.* 2019a; Yang *et al.* 2019a; Li *et al.* 2019b). Several models such as N-wards subduction (Xu *et al.* 1994; Song *et al.* 2013; Huang *et al.* 2015; Yang *et al.* 2015; Cui *et al.* 2019; Fu *et al.* 2020), S-wards subduction (Gehrels *et al.* 2011; Li *et al.* 2018c), double subduction (Wu *et al.* 2010; Zhang *et al.* 2015; Wang *et al.* 2018a) and multiple-accretionary (Yan *et al.* 2007, 2010; Xiao *et al.* 2009) have been proposed to explain the subduction history of the Proto-Tethyan Ocean during the Cambrian–Ordovician period. However, the collisional timing between these micro-blocks and subsequent tectonic evolution (Late Ordovician – Silurian) are still in debate. For example, Zhang *et al.* (2017) studied the Silurian (440–414 Ma) intrusive magmatism in the North Qilian and suggested that < 445 Ma magmatism was formed in a post-collisional setting. Huang *et al.* (2015) performed Nd–Hf isotope modelling to test the role

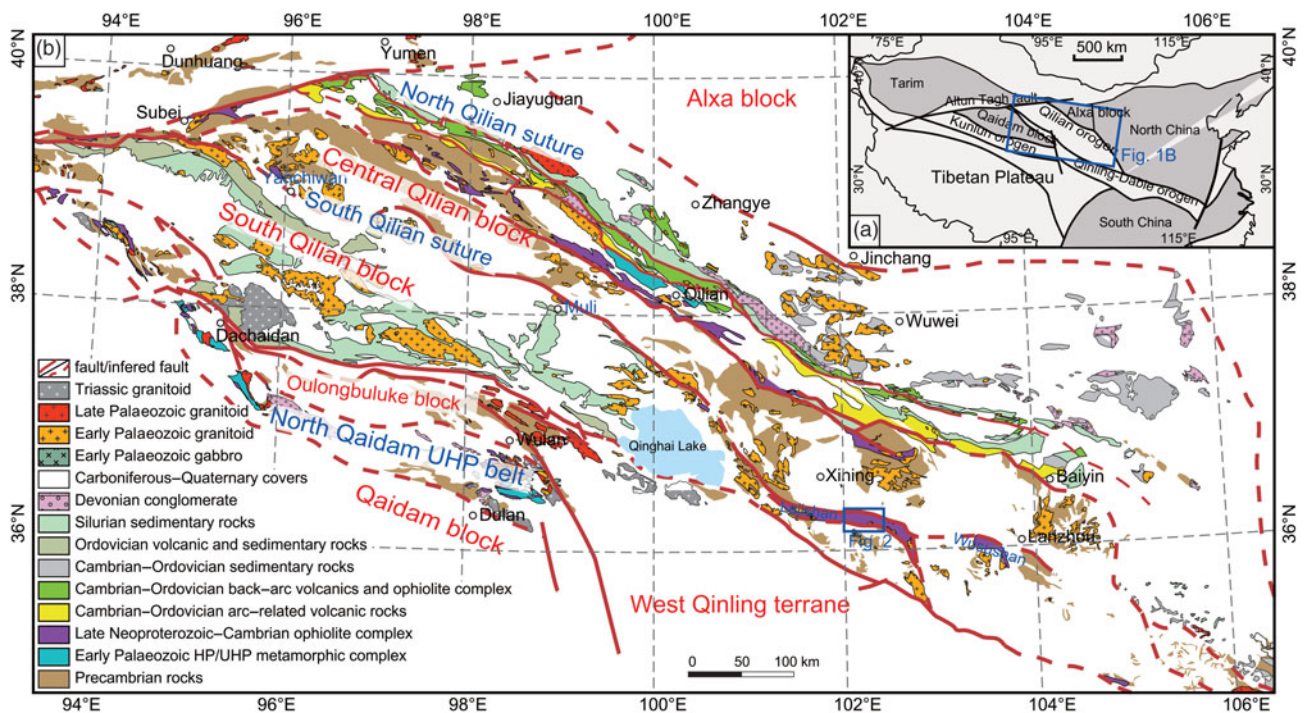


Fig. 1. (Colour online) (a) Tectonic framework of China and location of the Qilian Orogen, NW China. (b) Geological map of the Qilian Orogen and the location of study area (modified after Fu *et al.* 2018a, 2020).

of Archaean basement in the formation of *c.* 450 Ma magmatism within the Central Qilian and South Qilian blocks, and further suggested that the Late Ordovician igneous rocks (*c.* 450 Ma) were the products in response to the closure of the Proto-Tethyan Ocean. However, Li *et al.* (2018b) suggested that the lower Silurian andesitic-dacitic volcanic rocks in Yanjiasi-Chenjihae regions were formed in continental arc and back-arc settings during the S-wards subduction of the North Qilian Ocean, implying that the closure of the Proto-Tethyan Ocean was not finished before 438 Ma. An understanding of the tectonic setting of these Upper Ordovician–Silurian igneous rocks is therefore critical to decipher the evolutionary history of the Qilian Orogen.

The South Qilian suture is located between the Central Qilian and South Qilian blocks and contains relics of the early Palaeozoic intra-oceanic trench-arc system which recorded the subduction history of the South Qilian Ocean (southern branch of the Proto-Tethyan Ocean in the Qilian Orogen; Yan *et al.* 2019a; Fu *et al.* 2018a, 2019b). In this district, Upper Ordovician volcanic rocks and Upper Ordovician–Silurian fluvial sedimentary rocks have been reported and considered as the result of the collision between the microcontinental blocks. However, the Silurian igneous rocks have not been identified and recognized before, leading to the absence of tectonic evolution during the Silurian period. In this study, we report newly recognized lower Silurian subvolcanic rocks from the Lajishan district within the South Qilian suture zone. Zircon laser ablation inductively coupled plasma mass spectrometry (LA-ICP-MS) U–Pb ages, whole-rock major- and trace-element data and Sr–Nd isotopic compositions are presented to better understand the petrogenesis of these subvolcanic rocks. Combined with knowledge of regional geology, the tectonic setting and implications are discussed to further constrain the evolutionary history and closure timing of the South Qilian Ocean.

2. Regional geological setting

The Qilian orogenic belt is a pronounced orogenic collage of the Tethyan tectonic domain in the NE Tibetan Plateau and is bounded by the Altyn–Tagh Fault to the west, a Cenozoic basin along the Qinling–Dabie orogen to the SE and the Longshoushan Fault to the NE (see Fig. 1a). It mainly consists of two suture zones (the North Qilian and South Qilian suture zones), which separate the Central Qilian block and the South Qilian block (see Fig. 1b; Xiao *et al.* 2009; Gehrels *et al.* 2011; Yan *et al.* 2015; Zhang *et al.* 2015a; Xia *et al.* 2016; Fu *et al.* 2018a, 2019b; Li *et al.* 2018a; Zuza *et al.* 2018). The Central Qilian and South Qilian blocks are mainly composed of Precambrian lower greenschist- to amphibolite-facies metamorphic rocks and considered as microcontinental fragments which rifted from South China (Wan *et al.* 2003, 2006; Tung *et al.* 2012; Yan *et al.* 2015; Li *et al.* 2018c, 2020). In other literature, the South Qilian block was usually considered as a wide subduction–accretion complex named the South Qilian Belt (Song *et al.* 2014; Zhang *et al.* 2017b) as a result of the discovery of numerous arc-like volcanic rocks and Silurian flysch related to subduction (Yan *et al.* 2015).

Systematic lithological, geochemical and geochronological studies indicated that the South Qilian Block was accreted to the south margin of the Central Qilian Block during the early Palaeozoic Era (Xiao *et al.* 2009; Yan *et al.* 2015, 2020; Fu *et al.* 2019b). It was then intruded by later subduction-related igneous rocks (arc-like volcanic rocks and gabbros) and overlain by Silurian flysch that covered the central part of the South Qilian Block (Fig. 2). We suggest that it is mainly composed of Precambrian base (Ma *et al.* 2017; Fu *et al.* 2019b; Li *et al.* 2019a) and was accreted to the Central Qilian Block during early Palaeozoic time. Later igneous rocks and Silurian flysch associated with subduction and collision developed and overlapped on the Precambrian base. We therefore named this the South Qilian Block.

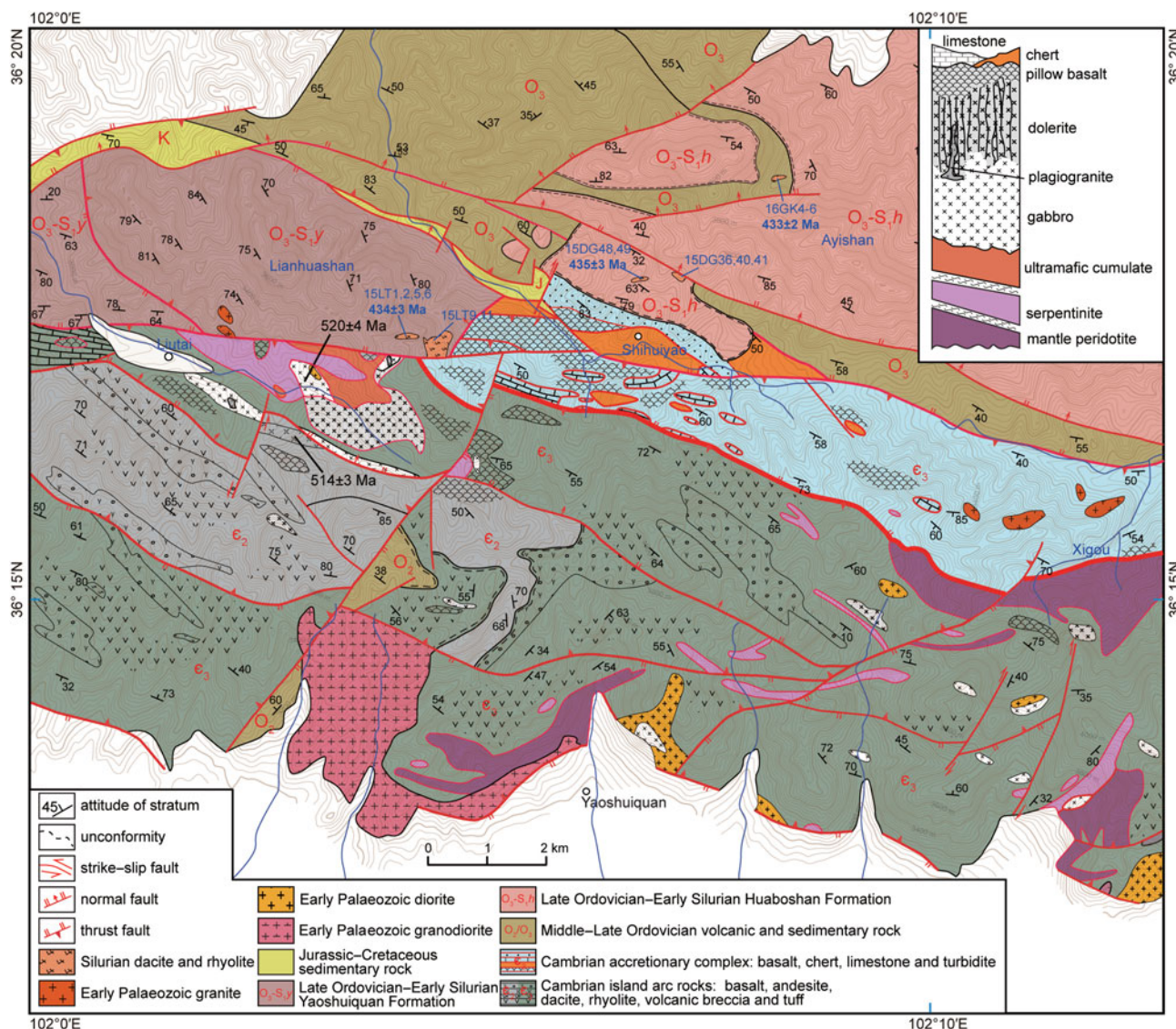


Fig. 2. (Colour online) Geological map of the central part of the South Qilian suture with sampling localities and ages (modified after Fu *et al.* 2018a; Yan *et al.* 2019a).

The North Qilian suture zone is dominated by a typical Marianan-type intra-oceanic subduction system including accretionary complex, ophiolite, seamount, island arc and back-arc/fore-arc basins (Xiao *et al.* 2009; Tseng *et al.* 2009; Wu *et al.* 2010; Yan *et al.* 2010; Yang *et al.* 2012; Song *et al.* 2013; Zhang *et al.* 2017a), which have been extensively studied in previous literature. The South Qilian suture zone is mainly composed of Cambrian ophiolite complex and volcano-sedimentary rocks, Ordovician intrusive and volcanic rocks, and latest Ordovician–Silurian sedimentary rocks (Wang & Liu, 1976; Qiu *et al.* 1995; Yang *et al.* 2002; Wang *et al.* 2018b; Fu *et al.* 2014, 2018a, 2019b; Zhang *et al.* 2019). These rocks are exposed discontinuously along the northern margin of the South Qilian Block and are preserved in the Lajishan area (Fig. 1b); other researchers (e.g. Qinghai Geological Survey Institute) also referred to the South Qilian suture as the Lajishan suture (Wang & Liu 1976; Fu *et al.* 2018a; Yan *et al.* 2019b). In this district, the Cambrian ophiolite complex is typical of a super-subduction zone ophiolite, which is composed of ultramafic rocks (e.g. amphibolite, peridotite and serpentinite), gabbro, plagiogranite, dolerite and pillow lava as revealed by the stratigraphic column of ophiolite complex in Figure 2 (Fu *et al.* 2018a, 2019a; Yan *et al.* 2019a).

The Cambrian volcano-sedimentary rocks contain pillow basalt, chert, limestone, mélange, tuff, massive basalt, andesite and dacite, representing a dismembered intra-oceanic arc-accretionary complex (Fu *et al.* 2018b, 2019a; Yan *et al.* 2019a, b). The Ordovician intrusive rocks (including diorite, granodiorite and granite) intrude the Cambrian arc-accretionary complex and are interpreted as being associated with subduction and/or collision (Fu *et al.* 2018a; Cui *et al.* 2019). The Upper Ordovician volcanic rocks (andesite, tuff and volcanic breccia) are considered to have been generated in a collisional setting (Sun *et al.* 2019). Further, the strata described above are non-conformably overlain by the latest Ordovician–Silurian sedimentary rocks that are mainly distributed along the northern margin of the South Qilian suture.

3. Sampling, field and petrographic descriptions

Thirteen subvolcanic samples with slight alteration were collected from Lianhuashan (15LT1, 15LT2, 15LT5, 15LT9, 15LT11), Ayishan (16GK4, 16GK5, 16GK6) and Shihuiyao (15DG36, 15DG48, 15DG49, 15DG40, 15DG41) in the South Qilian suture, and we also collected one sample c. 3.5 m from a subvolcanic dyke;

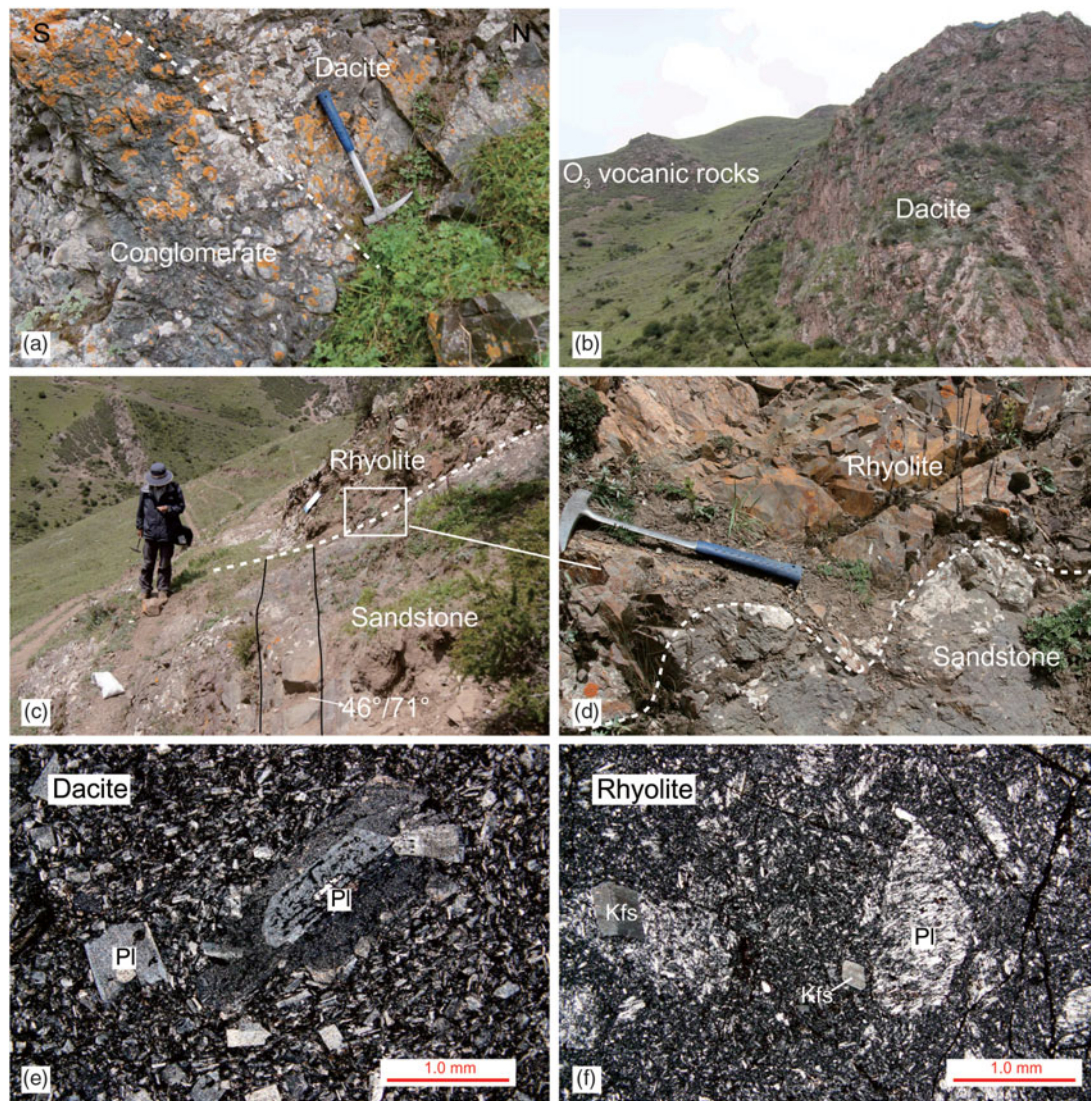


Fig. 3. (Colour online) Representative photographs of field relationships and photomicrographs of the lower Silurian subvolcanic rocks from the South Qilian suture. (a) Lianhuashan dacites intruded conglomerate of the Yaoshuiquan formation ($36^{\circ} 17' 15.7''$ N, $102^{\circ} 4' 12.4''$ E); (b) Ayishan dacites intruded the Upper Ordovician volcanic rocks ($36^{\circ} 18' 41.4''$ N, $102^{\circ} 8' 24.7''$ E); (c, d) Shihuiyao rhyolites intruded sandstone of the Huabaoshan formation ($36^{\circ} 17' 40.1''$ N, $102^{\circ} 6' 45.7''$ E); (e, f) photomicrographs under cross-polarized transmitted light, exhibiting obvious porphyritic texture comprising euhedral/subhedral phenocrysts and matrix; the phenocryst minerals mainly comprise plagioclase and minor K-feldspar. The size of the phenocrysts ranges over 0.10–1.6 mm. The matrix is mainly composed of plagioclase microlites and cryptocrystalline-glassy materials. Kfs – K-feldspar; Pl – plagioclase.

the sampling locations are shown in Figure 2. Based on the observations of field outcrops, hand specimens and photomicrographs, we classify these samples into two types of subvolcanic rocks, dacite and rhyolite, respectively. At Lianhuashan, dacite dykes with a near-EW trend intrude O_3 - S_1 sedimentary strata of the Yaoshuiquan formation. These dykes range in thickness from 3 to 15 m and have lateral extents of 20–80 m. They have sharp contacts with their host rocks (Fig. 3a). They are grey in colour and fine-grained, with plagioclase phenocrysts visible in hand specimens. We collected five samples from two different dykes (Fig. 2). At Ayishan, dacite dykes with a near-EW trend intrude Upper Ordovician volcanic rocks. These dykes range in thickness from c. 12 to 21 m and have lateral extents of c. 60 m. They have sharp contacts with their host rocks (Fig. 3b). They are light-grey in colour and fine-grained, with plagioclase phenocrysts visible in hand specimens. We collected three samples from one dyke. At Shihuiyao, rhyolite dykes with a near NW trend intrude O_3 - S_1 sedimentary strata of the Huabaoshan

formation. These dykes range in thickness from 1 to 10 m and have lateral extents of 20–60 m. They have sharp contacts with their host rocks (Fig. 3c, d). They are white grey in colour and fine-grained, with plagioclase and K-feldspar phenocrysts visible in hand specimens. We collected five samples from two different dykes (Fig. 2).

Dacites exhibit a typical porphyritic texture consisting of euhedral/subhedral phenocryst and matrix. The subhedral phenocrysts of plagioclase (1.6–0.10 mm) are more than 90 vol.%, whereas the matrix are less than 10 vol.% and comprise plagioclase microlites and cryptocrystalline-glassy materials (opaque minerals in Fig. 3e). Some of plagioclase phenocrysts have cores surrounded by altered or reacted rims. These rhyolites are grey-white and reveal a porphyritic texture as shown by photomicrograph under cross-polarized light. They also have subhedral phenocrysts comprising plagioclase and K-feldspar, and matrix consisting of plagioclase microlites and cryptocrystalline-glassy materials (Fig. 3f). No hydrous minerals (e.g. biotite, amphibole) were found in these subvolcanic rocks.

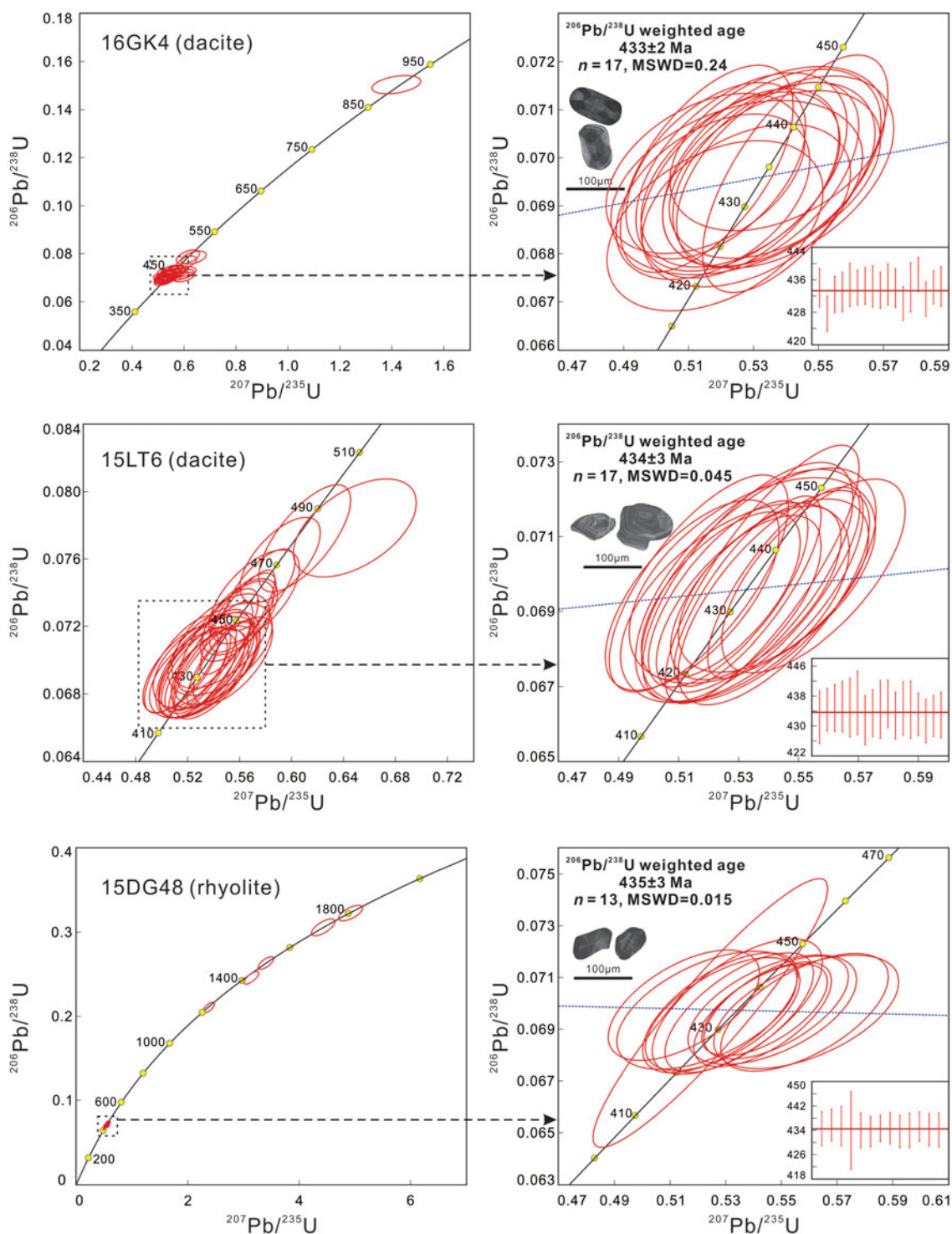


Fig. 4. (Colour online) U–Pb concordia diagrams for dacites (16GK4, 15LT6) and rhyolite (15DG48) from the South Qilian suture. CL images of representative grains are also shown.

4. Analytical methods

4.a. Zircon U–Pb dating

To determine the intrusion age of subvolcanic rocks, we collected three representative samples (15LT6, 16GK4, 15DG48) on which to perform LA-ICP-MS U–Pb dating of zircons. Zircon grains were separated from these samples using heavy-liquid and magnetic separation techniques. The separated zircons were hand-picked

under a binocular microscope and mounted in epoxy resin, and were then polished to expose the centres of the zircon grains. To visualize the internal structure and select potential targets for U–Pb analysis, cathodeluminescence (CL) images (Fig. 4) were obtained using a scanning electron microscope at Beijing Createch Testing Technology Co. Ltd. Measurement of U, Th and Pb isotopes was performed using an Agilent 7500a LA-ICP-MS. An ESI NWR 193-nm laser-ablation system and an

AnalytikJena PQMS Elite ICP-MS were combined for the experiments. A beam size of 25 μm was used for all samples. Zircon 91500 and Si in NIST SRM 610 were used for external calibration, and Zr was used as the internal standard (Liu *et al.* 2010). Detailed protocols and analytical methods are described in Li *et al.* (2009). Off-line raw data selection, the integration of background and analytical signals, and time-drift correction and quantitative calibration for U–Pb dating were all performed using ICP-MS DataCal (Liu *et al.* 2010). Measured compositions were corrected for common Pb using non-radiogenic ^{204}Pb , but corrections were found to be sufficiently small to be insensitive to the choice of common Pb composition. An average value of the present-day crustal composition ($^{206}\text{Pb}/^{204}\text{Pb}=18.700$; Stacey & Kramers, 1975) was therefore used for the common Pb correction (assuming that common Pb is largely related to surface contamination introduced during sample preparation). Uncertainties on individual analyses are included in the data tables and are reported at a 1σ level. Mean ages for pooled U/Pb (and Pb/Pb) analyses are quoted within the 95% confidence interval. Data reduction was conducted using the Isoplot/Ex v. 3.0 program (Ludwig, 2001).

4.b. Whole-rock major and trace elements

Thirteen subvolcanic rock samples were chosen for analysis of major and trace elements and then pulverized to less than 200 mesh. A Phillips PW4400 sequential X-ray fluorescence spectrometer (XRF) with Rh-anode tube was used to measure the major-element oxides at the National Research Center for Geoanalysis, Chinese Academy of Geological Sciences, following the detailed analytical methods described in the article by Liu *et al.* (2008). All major-element oxide concentrations are reported on a volatile-free basis. Detection limits are $< 0.01\%$ for major elements. Trace elements, including rare earth elements (REEs), were fused-glassed dissolved in nitric acid, and measured by ICP-MS using a VG Elemental PQII Plus system. Rh was added as an internal standard to 1% HNO_3 following the procedures of Liang *et al.* (2000). The international standard reference materials (e.g. GSR1 and GSR3) were used to monitor the stability and accuracy of the instrument during analyses. Accuracy and precision of the data are better than 5% for trace elements.

4.c. Sr–Nd isotopic analysis

Five subvolcanic rock samples from the South Qilian suture were chosen for Sr and Nd isotopic analyses. Firstly, sample powders were dissolved in an acidic mixture of HNO_3 (1 mL), and HF (4 mL) in Teflon bombs on a hotplate at 150°C for 48 hours. The acid was then dried to incipient dryness and the digestion process was repeated. Solutions were separated by cation and HDEHP-coated columns using conventional cation-exchange techniques. We followed the procedures described by Li *et al.* (2012) for sample preparation and chemical separation. Sr–Nd isotopic measurements were performed on a Thermo Fisher Scientific Neptune Plus MC-ICP-MS at the Beijing Createch Testing Technology Co. Ltd. Mass fractionation corrections for Sr and Nd isotopic ratios are based on $^{86}\text{Sr}/^{88}\text{Sr} = 0.1194$ and $^{146}\text{Nd}/^{144}\text{Nd} = 0.7219$, respectively. The $^{87}\text{Sr}/^{86}\text{Sr}$ ratio of the NIST SRM 987 (formerly NBS 987) Sr standard was 0.710258 ± 7 (2σ), and the measured $^{143}\text{Nd}/^{144}\text{Nd}$ ratios of the La Jolla and JNDI-1 Nd standard solutions were 0.511841 ± 3 (2σ) and 0.512104 ± 5 (2σ), respectively (Tanaka *et al.* 2000; Weis *et al.* 2006).

5. Results

5.a. Zircon U–Pb ages

Three representational samples (16GK4, 15LT6, 15DG48) were selected from subvolcanic rocks in the South Qilian suture for zircon U–Pb dating. Complete U–Pb isotopic data for these zircons are presented in Table 1. LA-ICP-MS data for 16GK4, 15LT6 and 15DG48 yielded weighted mean average $^{206}\text{Pb}/^{238}\text{U}$ ages of 433 ± 2 Ma (1σ ; mean square weighted deviation (MSWD), 0.24), 434 ± 3 Ma (1σ ; MSWD, 0.045) and 435 ± 3 Ma (1σ ; MSWD, 0.015) (Fig. 4), respectively. All of the analysed spots have high U (176–2631 ppm) and Th (32.7–856 ppm) contents with relative low Th/U ratios of 0.01–1.58 (mostly greater than 0.1), which suggests that these zircons have a magmatic origin (Belousova *et al.* 2002; Wu *et al.* 2004). This is also supported by the scallop-like and oscillatory zoning texture in CL image (Fig. 4). Some inherited zircon grains in these samples were dated. Most of the inherited zircons are of Ordovician – early Silurian age with $^{206}\text{Pb}/^{238}\text{U}$ ages ranging from 440 to 486 Ma. Five analyses from 15LT6 yield older $^{206}\text{Pb}/^{238}\text{U}$ ages of 1231–1803 Ma (late Palaeoproterozoic to Mesoproterozoic) and one analysis from 15GK4 gave a slightly older $^{206}\text{Pb}/^{238}\text{U}$ age of 903 Ma (Neoproterozoic). The $^{206}\text{Pb}/^{238}\text{U}$ ages are not correlated with U content (Fig. 5), suggesting that ages are not affected by the high U-matrix affect and radiation damage (White & Ireland, 2012; Gao *et al.* 2014). We therefore interpret these zircon U–Pb ages as the intrusion time of the subvolcanic rocks in the South Qilian suture.

5.b. Major- and trace-element geochemistry

Data for major and trace elements of 13 subvolcanic rock samples are listed in Table 2. In the $\text{K}_2\text{O}+\text{Na}_2\text{O}$ versus SiO_2 (TAS) diagram (Fig. 6a), samples are classified into dacites and rhyolites with loss-on-ignition (LOI) values ranging from 0.70 to 4.30 wt%. The samples of dacite display SiO_2 (61.43–65.13 wt%), high Al_2O_3 (15.76–19.11 wt%) and $\text{Fe}_2\text{O}_3^{\text{T}}$ (3.46–4.42 wt%), and low MgO (0.85–1.36 wt%) and Mg no. (29.05–39.97). Instead, the samples of rhyolite have low K_2O (0.09–3.81 wt%) concentrations and higher $\text{K}_2\text{O}/\text{Na}_2\text{O}$ ratios (0.01–0.64). Most samples fall in the high-K calc-alkaline and calc-alkaline fields in the $\text{K}_2\text{O}-\text{SiO}_2$ diagram (Fig. 6b), and all show weakly metaluminous–peraluminous affinity with A/CNK indexes of 0.92–1.20 in the A/CNK–A/NK diagram (Fig. 6c). Notably, the dacites are enriched in Sr (278–640 ppm), low in Y (5.11–14.7 ppm, < 18 ppm) and Yb (0.29–1.39 ppm, < 1.9 ppm), and have high Sr/Y (32.26–76.84) and La/Yb (27.84–115.55, > 20) ratios, which are typical characteristics of adakites defined by Defant & Drummond (1990). All samples of dacite are plotted in the adakite zone in the Sr/Y versus Y diagram (Fig. 6d), indicating that dacites are adakitic rocks. All subvolcanic rocks display slight to high fractionation between light REE (LREE) and heavy REE (HREE) ($\text{La}_\text{N}/\text{Yb}_\text{N} = 19.97\text{--}225.95$) and weakly negative to weakly positive Eu anomalies ($\delta\text{Eu} = 0.90\text{--}1.52$; Fig. 7a). They exhibit relative depletion in high-field-strength elements (HFSEs; Nb, Ta, P, Ti) in the primitive-mantle-normalized trace-element spider diagram (e.g. Fig. 7b). Furthermore, they show three different patterns in REEs and the trace-element spider diagram (Fig. 7a, b). The dacites collected from Lianhuashan have relative flat REE patterns with low LREE/HREE ratios (14.85–15.88), whereas the rhyolites collected from Shihuiyao have high fractionation with greater LREE/HREE ratios (28.19–57.24), indicating they may have experienced different magmatic processes or originated from various sources.

Table 1. LA-ICP-MS U–Pb isotopic compositions and ages of zircon from the lower Silurian subvolcanic rocks of the South Qilian suture

Spot no.	Concentration (ppm)				Isotope ratio						Age (Ma)			
	Pb*	Th	U	Th/U	²⁰⁷ Pb/ ²⁰⁶ Pb	1σ	²⁰⁷ Pb/ ²³⁵ U	1σ	²⁰⁶ Pb/ ²³⁸ U	1σ	²⁰⁷ Pb/ ²³⁵ U	1σ	²⁰⁶ Pb/ ²³⁸ U	1σ
16GK4-01	72.7	228	932	0.24	0.0553	0.0018	0.5491	0.0195	0.0713	0.0008	444	12.8	444	5.1
16GK4-02	67.5	175	922	0.19	0.0553	0.0014	0.5423	0.0133	0.0709	0.0008	440	8.7	442	4.9
16GK4-03	128	463	1749	0.26	0.0548	0.0015	0.5413	0.0113	0.0710	0.0009	439	7.5	442	5.2
16GK4-04	45.1	253	505	0.50	0.0563	0.0027	0.5514	0.0283	0.0707	0.0008	446	18.5	441	4.8
16GK4-05	65.9	151	851	0.18	0.0576	0.0013	0.6094	0.0160	0.0763	0.0011	483	10.1	474	6.5
16GK4-06	67.0	265	859	0.31	0.0556	0.0014	0.5347	0.0134	0.0697	0.0008	435	8.9	434	4.7
16GK4-07	50.9	107	732	0.15	0.0546	0.0014	0.5182	0.0136	0.0686	0.0007	424	9.1	428	4.4
16GK4-08	35.1	55.3	483	0.11	0.0561	0.0015	0.5642	0.0156	0.0727	0.0008	454	10.1	453	5.1
16GK4-09	108	338	1439	0.23	0.0548	0.0017	0.5249	0.0158	0.0694	0.0007	428	10.6	432	4.5
16GK4-10	66.9	133	972	0.14	0.0549	0.0013	0.5258	0.0125	0.0695	0.0008	429	8.3	433	4.9
16GK4-13	186	485	2631	0.18	0.0535	0.0010	0.5156	0.0109	0.0698	0.0009	422	7.3	435	5.3
16GK4-14	73.6	343	906	0.38	0.0558	0.0014	0.5366	0.0133	0.0697	0.0007	436	8.8	434	4.3
16GK4-15	43.3	52.5	602	0.09	0.0555	0.0017	0.5610	0.0199	0.0730	0.0009	452	12.9	454	5.6
16GK4-17	30.2	189	329	0.57	0.0553	0.0020	0.5378	0.0190	0.0707	0.0008	437	12.5	440	4.7
16GK4-18	44.4	41.3	592	0.07	0.0563	0.0015	0.6151	0.0184	0.0787	0.0012	487	11.6	488	7.0
16GK4-19	181	503	2500	0.20	0.0534	0.0011	0.5184	0.0113	0.0697	0.0007	424	7.6	435	4.5
16GK4-20	311	52.2	4621	0.01	0.0612	0.0013	0.6079	0.0128	0.0715	0.0008	482	8.1	445	4.6
16GK4-21	97.1	134	595	0.23	0.0670	0.0020	1.4180	0.0385	0.1504	0.0015	897	16.2	903	8.7
16GK4-22	35.2	0.444	516	0.00	0.0560	0.0025	0.5730	0.0308	0.0725	0.0009	460	19.9	451	5.7
16GK4-23	54.3	126	735	0.17	0.0608	0.0017	0.5977	0.0168	0.0703	0.0008	476	10.7	438	5.0
16GK4-25	98.2	445	1238	0.36	0.0542	0.0015	0.5263	0.0133	0.0697	0.0008	429	8.8	434	5.1
16GK4-27	29.9	87.3	346	0.25	0.0583	0.0018	0.6377	0.0198	0.0784	0.0011	501	12.3	486	6.6
16GK4-28	55.2	106	800	0.13	0.0543	0.0014	0.5260	0.0125	0.0695	0.0007	429	8.3	433	4.5
16GK4-30	32.9	49.6	486	0.10	0.0555	0.0016	0.5357	0.0137	0.0698	0.0008	436	9.1	435	5.1
16GK4-31	99.6	235	1439	0.16	0.0552	0.0012	0.5344	0.0115	0.0696	0.0008	435	7.6	434	4.8
16GK4-32	110	413	1487	0.28	0.0553	0.0016	0.5278	0.0131	0.0690	0.0007	430	8.7	430	4.2
16GK4-33	24.9	143	279	0.51	0.0571	0.0017	0.5699	0.0163	0.0722	0.0008	458	10.6	449	4.7
16GK4-34	117	32.7	1897	0.02	0.0562	0.0011	0.5429	0.0117	0.0697	0.0010	440	7.7	434	6.1
16GK4-35	34.3	69.5	489	0.14	0.0553	0.0016	0.5374	0.0135	0.0702	0.0007	437	8.9	437	4.2
16GK4-36	31.9	51.0	436	0.12	0.0547	0.0014	0.5592	0.0151	0.0735	0.0007	451	9.8	457	4.3
16GK4-37	32.3	53.4	484	0.11	0.0540	0.0013	0.5175	0.0122	0.0692	0.0007	424	8.2	431	4.2
16GK4-38	26.8	51.7	394	0.13	0.0534	0.0013	0.5152	0.0125	0.0697	0.0007	422	8.4	434	4.1
16GK4-39	25.0	97.3	315	0.31	0.0547	0.0016	0.5443	0.0166	0.0718	0.0008	441	10.9	447	4.8
16GK4-40	24.3	53.8	353	0.15	0.0559	0.0014	0.5392	0.0139	0.0697	0.0008	438	9.2	434	4.9
15LT6-1	167	237	573	0.41	0.0566	0.0013	0.5418	0.0130	0.0694	0.0012	440	8.6	432	7.1
15LT6-2	183	259	632	0.41	0.0563	0.0014	0.5417	0.0130	0.0697	0.0009	440	8.5	434	5.7
15LT6-3	234	333	797	0.42	0.0560	0.0011	0.5625	0.0105	0.0728	0.0010	453	6.8	453	5.7
15LT6-4	236	317	820	0.39	0.0563	0.0012	0.5913	0.0126	0.0759	0.0010	472	8.1	472	6.2
15LT6-5	209	310	587	0.53	0.0558	0.0012	0.5581	0.0116	0.0723	0.0010	450	7.5	450	5.8
15LT6-6	249	360	835	0.43	0.0566	0.0011	0.5451	0.0104	0.0698	0.0010	442	6.8	435	6.3
15LT6-7	158	255	368	0.69	0.0553	0.0017	0.5346	0.0168	0.0698	0.0011	435	11.1	435	6.8

(Continued)

Table 1. (Continued)

Spot no.	Concentration (ppm)				Isotope ratio						Age (Ma)			
	Pb*	Th	U	Th/U	$^{207}\text{Pb}/^{206}\text{Pb}$	1σ	$^{207}\text{Pb}/^{235}\text{U}$	1σ	$^{206}\text{Pb}/^{238}\text{U}$	1σ	$^{207}\text{Pb}/^{235}\text{U}$	1σ	$^{206}\text{Pb}/^{238}\text{U}$	1σ
15LT6-8	201	292	633	0.46	0.0564	0.0015	0.5586	0.0117	0.0722	0.0013	451	7.7	450	7.6
15LT6-9	67.8	96.5	258	0.37	0.0553	0.0015	0.5457	0.0154	0.0711	0.0011	442	10.1	443	6.9
15LT6-10	109	143	273	0.53	0.0602	0.0018	0.6489	0.0194	0.0778	0.0012	508	11.9	483	7.1
15LT6-11	129	198	436	0.45	0.0552	0.0015	0.5331	0.0143	0.0698	0.0013	434	9.5	435	7.9
15LT6-12	292	410	985	0.42	0.0560	0.0016	0.5379	0.0132	0.0700	0.0014	437	8.7	436	8.5
15LT6-13	72.6	112	176	0.63	0.0555	0.0018	0.5288	0.0156	0.0692	0.0011	431	10.4	432	6.6
15LT6-14	223	290	653	0.44	0.0570	0.0013	0.6102	0.0145	0.0772	0.0013	484	9.1	480	7.8
15LT6-15	370	553	1044	0.53	0.0552	0.0012	0.5436	0.0126	0.0712	0.0012	441	8.3	443	7.5
15LT6-16	529	856	1288	0.66	0.0554	0.0010	0.5331	0.0100	0.0695	0.0010	434	6.6	433	6.3
15LT6-17	78.2	109	289	0.38	0.0560	0.0018	0.5368	0.0160	0.0697	0.0013	436	10.6	434	7.7
15LT6-18	385	508	1222	0.42	0.0572	0.0011	0.5550	0.0125	0.0700	0.0011	448	8.2	436	6.4
15LT6-19	220	305	804	0.38	0.0536	0.0012	0.5146	0.0119	0.0694	0.0010	422	8.0	433	6.3
15LT6-20	332	462	910	0.51	0.0561	0.0019	0.5451	0.0164	0.0706	0.0011	442	10.8	440	6.7
15LT6-21	224	341	616	0.55	0.0536	0.0012	0.5167	0.0122	0.0698	0.0012	423	8.2	435	7.1
15LT6-22	175	241	591	0.41	0.0554	0.0016	0.5336	0.0155	0.0697	0.0013	434	10.3	434	7.6
15LT6-24	203	303	566	0.54	0.0558	0.0013	0.5358	0.0116	0.0695	0.0009	436	7.7	433	5.7
15LT6-25	221	310	777	0.40	0.0555	0.0012	0.5301	0.0112	0.0692	0.0010	432	7.5	431	5.8
15LT6-26	151	203	545	0.37	0.0547	0.0013	0.5241	0.0108	0.0694	0.0009	428	7.2	433	5.5
15LT6-27	258	353	821	0.43	0.0558	0.0012	0.5605	0.0118	0.0726	0.0009	452	7.7	452	5.5
15LT6-28	278	423	758	0.56	0.0549	0.0013	0.5266	0.0109	0.0695	0.0010	430	7.2	433	6.1
15LT6-29	525	794	1371	0.58	0.0560	0.0011	0.5756	0.0111	0.0742	0.0010	462	7.2	461	6.0
15LT6-30	222	317	605	0.52	0.0559	0.0015	0.5715	0.0142	0.0738	0.0011	459	9.2	459	6.8
15DG48-2	200	305	629	0.48	0.0543	0.0012	0.5233	0.0132	0.0697	0.0009	427	8.8	435	5.6
15DG48-3	192	301	597	0.50	0.0534	0.0011	0.5150	0.0111	0.0699	0.0009	422	7.5	436	5.3
15DG48-4	994	363	551	0.66	0.1104	0.0017	4.9266	0.0885	0.3227	0.0038	1807	15.2	1803	18.4
15DG48-5	1483	907	786	1.15	0.0818	0.0013	2.3785	0.0417	0.2104	0.0025	1236	12.6	1231	13.4
15DG48-6	177	273	554	0.49	0.0556	0.0013	0.5342	0.0125	0.0699	0.0011	435	8.3	435	6.4
15DG48-7	384	670	736	0.91	0.0547	0.0012	0.5245	0.0172	0.0696	0.0021	428	11.5	434	12.8
15DG48-8	125	197	291	0.68	0.0561	0.0017	0.5644	0.0171	0.0730	0.0010	454	11.1	454	5.8
15DG48-9	117	102	808	0.13	0.0558	0.0012	0.5639	0.0125	0.0732	0.0009	454	8.1	456	5.3
15DG48-10	642	290	449	0.65	0.0936	0.0016	3.4039	0.0567	0.2633	0.0030	1505	13.1	1507	15.4
15DG48-12	340	135	210	0.64	0.1049	0.0022	4.4340	0.0867	0.3058	0.0041	1719	16.2	1720	20.2
15DG48-13	313	475	913	0.52	0.0549	0.0013	0.5281	0.0114	0.0696	0.0009	431	7.6	434	5.7
15DG48-14	329	433	1534	0.28	0.0564	0.0011	0.5433	0.0101	0.0696	0.0008	441	6.7	434	5.0
15DG48-18	325	485	955	0.51	0.0564	0.0011	0.5440	0.0092	0.0697	0.0007	441	6.1	435	4.4
15DG48-19	180	258	502	0.51	0.0567	0.0013	0.5468	0.0124	0.0698	0.0009	443	8.1	435	5.2
15DG48-20	118	111	846	0.13	0.0549	0.0011	0.5289	0.0114	0.0696	0.0009	431	7.5	434	5.4
15DG48-21	389	593	1132	0.52	0.0556	0.0012	0.5349	0.0109	0.0696	0.0009	435	7.2	434	5.7
15DG48-23	186	168	1250	0.13	0.0556	0.0010	0.5617	0.0108	0.0731	0.0010	453	7.0	455	5.7
15DG48-24	1209	635	402	1.58	0.0925	0.0015	3.1433	0.0540	0.2457	0.0031	1443	13.3	1416	15.9
15DG48-25	392	661	841	0.79	0.0569	0.0012	0.5482	0.0106	0.0698	0.0008	444	7.0	435	4.9
15DG48-27	200	289	613	0.47	0.0565	0.0012	0.5668	0.0134	0.0725	0.0010	456	8.7	451	6.3
15DG48-28	228	381	585	0.65	0.0580	0.0013	0.5590	0.0136	0.0697	0.0009	451	8.9	434	5.4
15DG48-29	331	505	958	0.53	0.0580	0.0012	0.5584	0.0123	0.0697	0.0009	450	8.0	434	5.6

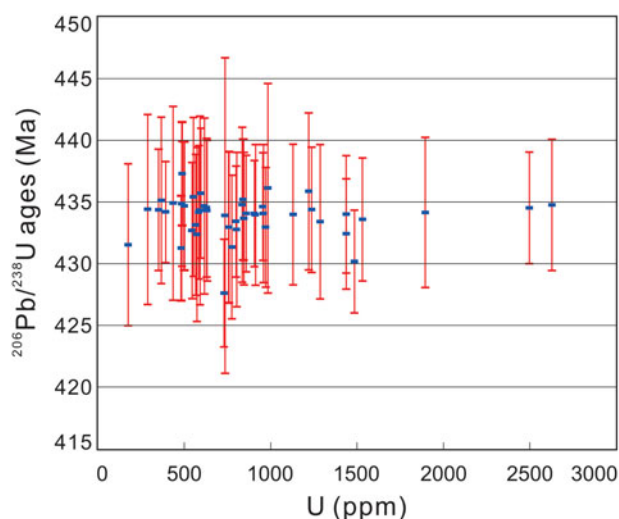


Fig. 5. (Colour online) Plot of zircon U versus $^{206}\text{Pb}/^{238}\text{U}$ ages for dacites and rhyolites from the South Qilian suture. $^{206}\text{Pb}/^{238}\text{U}$ ages are not correlated with U contents of these lower Silurian subvolcanic rocks, suggesting that they are not affected by the high-U matrix affect and radiation damage.

5.c. Sr–Nd isotope geochemistry

Data for the five subvolcanic rock samples chosen for Sr and Nd isotopic analyses are listed in Table 3. The initial $^{87}\text{Sr}/^{86}\text{Sr}$ ratios and $\epsilon_{\text{Nd}}(t)$ values were calculated at $t = 433$ Ma. In addition, we used the model proposed by DePaolo (1981) to calculate the depleted-mantle Nd model ages (T_{DM}). The results show that Sr–Nd isotopic compositions of the Lajishan subvolcanic rocks are characterized by relatively homogenous initial $^{87}\text{Sr}/^{86}\text{Sr}$ ratios of 0.7091 to 0.7138, and $\epsilon_{\text{Nd}}(t)$ values of -6.50 to -3.44 . The calculated values of the corresponding two-stage depleted-mantle Nd model ages ($T_{2\text{DM}}$) are 1.52–1.74 Ga, as listed in Table 3.

6. Discussion

6.a. Magmatic evolution of the lower Silurian subvolcanic rocks

The subvolcanic rocks (dacites and rhyolites) from the South Qilian suture have relatively low LOI values (0.70–4.30; average, 1.79; Table 2), indicating that the effect of alteration on the original chemical composition is negligible. We therefore suggest that the major- and trace-element data for these subvolcanic rocks can reflect their primary compositions. LOI-free data are plotted in all diagrams in this paper. There are two main mechanisms for the generation of intermediate-felsic melts: (1) fractional crystallization of mafic precursor magmas with or without assimilation of crustal materials into a magma chamber (Gertisser & Keller, 2000; Grove *et al.* 2003; Wanless *et al.* 2010); and (2) partial melting of previously emplaced volcanic, metamorphic or sedimentary rocks in the lower crust (Rapp & Watson, 1995; Dungan & Davidson, 2004; Annen *et al.* 2006). To understand the petrogenesis of Silurian subvolcanic rocks (dacites and rhyolites) in this study, we have to determine the mechanism that played the main role in their generation. Ma *et al.* (2015) performed the trace-element modelling to illustrate the role of crustal assimilation and fractional crystallization (AFC) processes in the petrogenesis of the high-Sr/Y lavas, and suggested that AFC or fractional crystallization (FC) processes would drive the magmas toward low Sr/Y and negative

Eu anomalies; this is the opposite of dacites with high Sr/Y ratios and no significantly negative Eu anomalies ($\text{Eu}/\text{Eu}^* = 0.90\text{--}1.08$) in this study. The process of AFC therefore cannot produce melts with high, adakite-like Sr/Y and La/Yb ratios, or could only have played a limited role, at least without substantially affecting the trace elements, during magma evolution (Castillo, 2012; Ma *et al.* 2015). In this study, adakite-like subvolcanic rocks (Lianhuashan and Ayishan dacites) with high Sr contents, Sr/Y and La/Yb ratios could have been directly derived from their respective sources (Castillo, 2012). The result is also supported by a simple Sr–Nd isotopic modelling for classical adakite contaminated/mixed with the upper continental crust (Fig. 8a), indicating that no crustal assimilation was involved in the formation of high Sr/Y dacites. Due to the low partition coefficients ($\ll 1.0$) of La and Sm (Adam & Green, 2006), the La/Sm ratio is extremely insensitive to partial melting process and can then be used to distinguish fractional crystallization and partial melting processes. Geochemical results show that partial melting has played a key role in the formation of Lianhuashan and Ayishan dacites, whereas fractional crystallization is important for the formation of Shihuiyao rhyolites from the South Qilian suture (Fig. 8b). A relatively constant range of Zr/Hf ratios for dacites and the obvious downward trend of rhyolites (Fig. 8c) probably suggest that no intensive fractional crystallization occurred in the magmatic evolution of dacites; however, the fractional crystallization of zircon may have taken place in the magmatic stage of Shihuiyao rhyolites. These results are also supported by the discriminant diagram (Fig. 8d), where dacites are plotted in the OGT (unfractionated M-, I- and S-type granite) area and rhyolites are in the FG (fractionated felsic granite) area. We therefore suggest that adakite-like dacites (Lianhuashan and Ayishan) might not have experienced AFC or FC processes, and were directly derived from the partial melting of their source regime. Instead, the Shihuiyao rhyolites may be the result of fractional crystallization (FC) of mafic precursor magmas without assimilation of crustal materials into their magma chamber. In Harker diagrams (Fig. 9), the Shihuiyao rhyolites reveal an obvious decrease in Fe_2O_3 , TiO_2 , P_2O_5 and MgO contents with increasing SiO_2 , indicating that they probably experienced fractional crystallization of Fe–Ti oxides and apatite. Furthermore, the plots of Ba versus Sr (Fig. 10a) and Ba versus Eu/Eu^* (Fig. 10b) indicate the mineral phase that played a dominant role in the formation of rhyolites. The results show that the fractional crystallization of K-feldspar and biotite took place.

6.b. Natural source and tectonic setting of the lower Silurian subvolcanic rocks

6.b.1. Natural source of the dacites

Except for the classical adakites derived from the partial melting of a subducting oceanic slab (Defant & Drummond, 1990; Martin *et al.* 2005), several other models have been proposed to decipher the genesis of adakitic rocks: (1) the partial melting of the mafic lower crust (Hou *et al.* 2004; Kay *et al.* 2005; Castillo, 2012; He *et al.* 2019); (2) crystal fractionation of arc-basaltic magmas at high pressure (Castillo *et al.* 1999; Rodriguez *et al.* 2007; Zhang *et al.* 2008); and (3) interaction between mantle peridotite and melts derived from lower crustal material delaminated into the mantle in both arc or non-arc tectonic environments (Xu *et al.* 2002; Castillo, 2006, 2012; Chen *et al.* 2013). The Lianhuashan dacites in this study show enrichment in Sr (442–640 ppm), depletion in Y (13.3–14.7 ppm) and Yb (1.34–1.39 ppm), and high Sr/Y ratios (32.26–45.66). These geochemical signatures are typical of adakitic

Table 2. Major- and trace-element compositions of the lower Silurian subvolcanic rocks of the South Qilian suture

Sampling locations	Lianhuashan					Ayishan			Shihuiyao				
	Lithology	Dacite	Dacite	Dacite	Dacite	Dacite	Dacite	Dacite	Rhyolite	Rhyolite	Rhyolite	Rhyolite	Rhyolite
Sample no.	15LT1	15LT2	15LT5	15LT9	15LT11	16GK4	16GK5	16GK6	15DG36	15DG48	15DG49	15DG40	15DG41
Major oxides													
SiO ₂	65.07	64.54	64.63	61.43	65.13	64.50	64.97	64.82	70.43	69.88	70.06	69.43	73.06
TiO ₂	0.45	0.46	0.45	0.50	0.46	0.45	0.45	0.50	0.23	0.24	0.26	0.27	0.14
Al ₂ O ₃	17.03	17.24	17.26	19.11	17.28	16.71	15.76	17.07	15.59	16.00	14.89	16.52	15.06
Fe ₂ O ₃ ^T	4.05	4.15	4.07	4.19	4.11	4.42	3.46	4.32	2.08	1.98	2.26	1.77	1.24
MnO	0.06	0.07	0.06	0.08	0.06	0.04	0.04	0.04	0.01	0.02	0.02	0.01	0.02
MgO	1.36	1.26	1.21	1.30	0.85	1.09	0.89	1.02	0.76	0.53	1.36	0.40	0.08
CaO	2.02	1.78	2.94	4.03	3.38	3.39	3.90	4.02	0.54	0.66	0.72	0.39	0.20
Na ₂ O	4.73	4.75	4.35	4.49	4.29	5.19	4.56	4.69	8.95	9.21	6.33	6.06	6.63
K ₂ O	2.85	3.09	2.83	1.57	2.68	1.87	2.32	2.04	0.14	0.09	2.49	3.81	2.69
P ₂ O ₅	0.19	0.19	0.19	0.17	0.18	0.15	0.15	0.16	0.07	0.05	0.09	0.07	0.03
LOI	1.89	1.91	1.45	2.38	1.28	2.58	4.30	1.95	1.09	1.14	1.54	1.00	0.70
Total	99.70	99.44	99.44	99.25	99.70	100.07	100.55	100.31	99.89	99.80	100.02	99.73	99.85
K ₂ O+Na ₂ O	7.75	8.04	7.33	0.35	0.62	7.25	7.14	6.84	9.20	9.43	8.96	10.00	9.40
K ₂ O/Na ₂ O	0.60	0.65	0.65	0.90	0.79	0.36	0.51	0.43	0.02	0.01	0.39	0.63	0.41
A/CNK	1.17	1.20	1.11	1.16	1.07	1.00	0.92	0.99	0.98	0.97	1.03	1.12	1.06
A/NK	1.74	1.69	1.85	2.57	1.91	1.92	1.81	2.03	1.58	1.59	1.36	1.29	1.30
CaO/Na ₂ O	0.43	0.37	0.68	0.90	0.79	0.65	0.86	0.86	0.06	0.07	0.11	0.06	0.03
Mg no.	39.97	37.55	37.05	38.05	29.05	32.83	33.67	31.84	41.96	34.65	54.43	30.87	11.31
σ	2.55	2.79	2.34	1.92	2.16	2.27	2.08	2.04	2.99	3.19	2.85	3.66	2.88
Trace elements													
Li	22.2	19.9	18.7	12.6	8.63	13.0	9.04	13.7	0.25	0.30	2.04	3.27	3.20
Sc	4.38	4.37	4.27	4.4	4.15	3.29	2.45	2.85	1.31	1.13	1.72	1.59	0.83
V	9.70	10.5	9.70	11.7	9.47	9.32	4.58	6.44	7.45	11.8	5.02	5.02	10.1
Cr	3.63	4.45	3.02	4.03	2.88	137	61.7	90.6	15.5	5.44	19.9	11.8	6.45
Co	5.04	5.15	4.79	5.25	5.13	7.07	5.00	5.93	2.50	2.22	2.95	1.35	1.88
Ni	1.77	1.87	2.03	3.07	2.21	35.1	14.7	20.1	9.13	4.56	12.2	4.46	16.6
Cu	10.0	8.03	10.2	13.5	7.3	13.5	6.36	15.5	5.45	9.29	9.37	26.0	25.0
Ga	20.8	21.2	20.6	24.1	20.3	26.7	22.7	27.9	23.0	22.5	15.4	23.8	18.8
Rb	111	115	94.4	59.8	86.5	78.2	85.9	76.6	4.17	4.75	107	216	103
Sr	492	442	598	640	621	416	278	365	52.4	58.3	79.6	360	198
Y	14.0	13.7	13.3	14.7	13.6	5.41	5.11	5.83	1.82	1.78	2.61	2.22	0.520
Zr	246	249	234	257	248	206	203	214	162	195	171	173	92.4
Nb	11.0	11.3	10.7	12.0	10.9	12.8	12.5	12.8	10.8	12.0	10.3	11.1	9.35
Cs	4.38	4.73	4.03	5.21	3.94	2.39	2.40	2.96	0.14	0.51	1.49	8.16	0.93
Ba	932	823	953	821	1077	569	630	629	23.1	27.3	293	1050	696
La	38.7	39.4	39.2	41.8	41.6	34.0	33.3	35.5	18.9	31.5	39.8	21.1	14.9
Ce	75.7	73.5	73.0	78.6	78.4	63.6	62.7	66.4	37.9	60.5	67.9	40.2	25.1
Pr	7.85	7.78	7.87	8.38	8.31	6.82	6.68	7.17	4.02	6.16	7.04	4.64	2.66
Nd	28.8	28.6	29.6	32.2	31.6	25.3	24.7	26.9	15.0	21.4	25.6	19.5	10.2

(Continued)

Table 2. (Continued)

Sampling locations Lithology	Lianhuashan					Ayishan			Shihuiyao				
	Dacite	Dacite	Dacite	Dacite	Dacite	Dacite	Dacite	Dacite	Rhyolite	Rhyolite	Rhyolite	Rhyolite	Rhyolite
Sm	4.52	4.52	4.44	4.81	4.76	4.30	4.15	4.59	2.65	3.16	3.60	3.29	1.55
Eu	1.21	1.20	1.25	1.38	1.24	1.33	1.27	1.41	0.79	0.92	1.00	0.93	0.54
Gd	3.66	3.71	3.90	3.78	3.66	3.30	3.15	3.54	1.58	1.81	2.12	2.01	0.760
Tb	0.48	0.50	0.51	0.50	0.50	0.34	0.33	0.37	0.15	0.17	0.20	0.18	0.06
Dy	2.72	2.48	2.51	2.76	2.58	1.31	1.26	1.44	0.51	0.54	0.70	0.62	0.43
Ho	0.52	0.47	0.50	0.52	0.52	0.19	0.17	0.20	0.07	0.08	0.09	0.09	0.07
Er	1.35	1.30	1.29	1.44	1.41	0.48	0.44	0.52	0.14	0.13	0.17	0.16	0.15
Tm	0.22	0.21	0.20	0.22	0.2	0.05	0.05	0.05	0.019	0.018	0.017	0.018	0.019
Yb	1.39	1.36	1.34	1.39	1.37	0.31	0.29	0.34	0.11	0.10	0.13	0.12	0.11
Lu	0.22	0.21	0.21	0.21	0.21	0.04	0.04	0.05	0.016	0.017	0.018	0.018	0.017
Hf	6.54	6.35	6.29	6.93	6.49	5.37	5.31	5.60	4.89	6.15	5.02	5.76	3.55
Ta	0.90	0.79	0.78	0.89	0.83	0.70	0.67	0.71	0.64	0.80	0.68	0.78	0.60
Pb	25.0	42.9	27.3	24.6	28.2	18.4	11.9	15.5	18.1	9.9	11.4	19.1	10.6
Th	13.6	12.4	12.7	13.7	13.1	9.50	9.23	9.80	8.58	10.2	9.24	9.97	6.21
U	3.54	3.33	3.37	3.01	3.31	2.96	2.50	2.95	3.42	3.37	2.94	2.96	2.21
ΣREE	167	165	166	178	176	141	138	148	81.8	126	148	92.8	55.9
LREE	157	155	155	167	166	135	133	142	79.3	124	145	89.7	55.0
HREE	10.56	10.24	10.46	10.82	10.45	6.02	5.73	6.50	2.56	2.83	3.41	3.18	0.96
LREE/HREE	14.85	15.14	14.85	15.45	15.88	22.48	23.19	21.82	30.96	43.69	42.50	28.19	57.24
δEu	0.91	0.90	0.92	0.99	0.91	1.08	1.08	1.07	1.18	1.18	1.11	1.11	1.52
δCe	1.06	1.03	1.02	1.03	1.03	1.02	1.03	1.02	1.07	1.06	0.99	1.00	0.98
Sr/Y	35.14	32.26	44.96	43.54	45.66	76.84	54.32	62.51	28.79	32.75	30.50	162.16	380.77
La/Y	2.76	2.88	2.95	2.84	3.06	6.29	6.52	6.08	10.38	17.70	15.25	9.50	28.65
Zr/Hf	37.61	39.21	37.20	37.09	38.21	38.49	38.12	38.30	33.13	31.71	34.06	30.03	26.03
Nb/Ta	12.22	14.30	13.72	13.48	13.13	18.37	18.53	17.98	16.88	15.00	15.15	14.23	15.58

Mg no. = 100 × molar MgO/(Mg + FeO^T), assuming FeO^T = 0.9 * Fe₂O₃^T

rocks. Due to different patterns of REE and trace-element distribution (Fig. 7a, b) for Lianhuashan and Ayishan dacites, we suggest that they may have different mechanisms of generation and be derived from different sources. Experimental studies suggest that the composition of source rocks plays a crucial role for generating adakitic melts with different geochemical characteristics (Castillo, 2012; Qian & Hermann, 2013; Ma *et al.* 2015). The Lianhuashan dacites have low Mg no. values (29.05–39.97) and low Ni (1.77–3.07 ppm; < 20 ppm) and Cr (2.88–4.45 ppm; < 10 ppm) contents, inconsistent with classical adakitic melts derived from subducting slabs (Defant & Drummond, 1990) but similar to melts derived from partial melting of mafic lower crust (Castillo, 2012; He *et al.* 2020). This is also supported by the high (⁸⁷Sr/⁸⁶Sr)_i (0.7091–0.7094) and low ε_{Nd}(*t*) values (–5.33 to –3.44), consistent with intrusive rocks derived from lower crust in the Qilian orogen (Zhang *et al.* 2006a, b; Tung *et al.* 2016).

Furthermore, as both Nb and Ta are immobile elements and are little affected by fractional crystallization or hydrothermal overprint in later geological events, the Nb/Ta ratios in magmatic rocks must have been inherited from their sources and can be

used to trace magma sources (Hawkesworth *et al.* 1993). As shown in Figure 7b, the negative Nb and Ti concentration anomalies rule out the origin of normal mid-ocean ridge basalt (N-MORB) or ocean-island basalt (OIB) -type sources in non-subduction zone environments, with associated melts characterized by typically positive Nb and Ti anomalies (e.g. Hofmann, 1997). The relatively low Nb/Ta ratios (12.22–14.30) of Lianhuashan dacites are similar to that of continental crust (average value, 13.4; Wedepohl, 1995), further supporting the conclusion that they are derived from partial melting of mafic lower crust. This result is also supported by the plots of CaO/(MgO+FeO^T+TiO₂) versus CaO+MgO+FeO^T+TiO₂ (Fig. 11a) and molar Al₂O₃/(MgO+FeO^T) versus Al₂O₃+MgO+FeO^T (Fig. 11b), where the Lianhuashan dacites are plotted within a mafic-rock-dominant source (amphibolite or metabasalt).

Although the Ayishan dacites also display adakitic geochemical characteristics with high Sr contents (278–416 ppm) and Sr/Y ratios (54.32–76.84), and lower Y (5.11–5.83 ppm) and Yb (0.29–0.34 ppm) contents, they have contents high of Ni (14.74–35.15 ppm; mostly > 20 ppm) and Cr (61.66–137.42 ppm; > 10 ppm), indicative of a

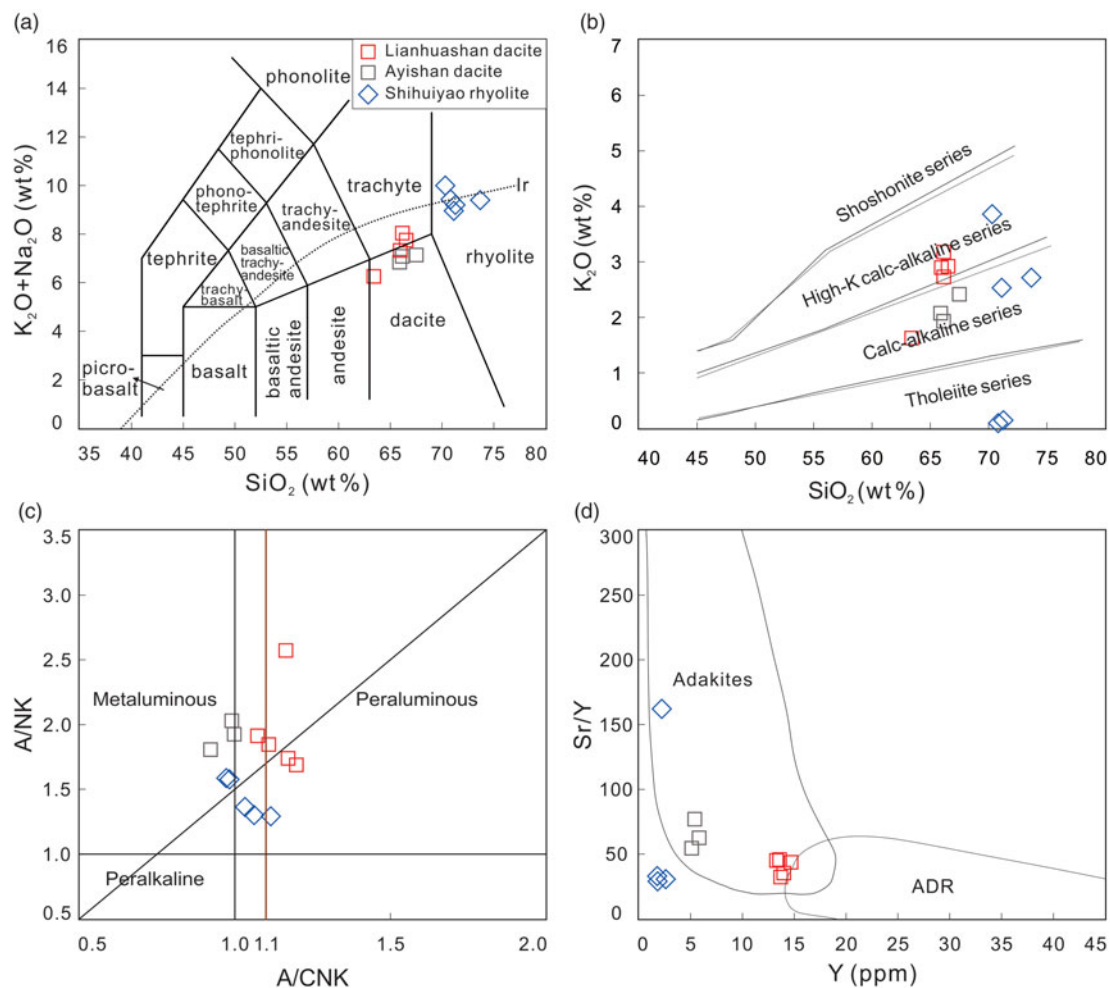


Fig. 6. (Colour online) Plots of (a) $(\text{K}_2\text{O} + \text{Na}_2\text{O})$ versus SiO_2 , (b) K_2O versus SiO_2 , (c) A/CNK versus A/NK and (d) Sr/Y versus Y of the lower Silurian subvolcanic rocks from the South Qilian suture. (d) Fields of adakites and classical island andesite–dacite–rhyolite (ADR) rocks are modified from Defant & Drummond (1990). All SiO_2 values are LOI-free.

mantle peridotite signature. However, the high $(^{87}\text{Sr}/^{86}\text{Sr})_i$ (0.7109–0.7110) and low $\epsilon_{\text{Nd}}(t)$ values (–6.50 to –6.28) rule out the theory that Ayishan dacites were derived from partial melting of peridotite mantle, which should have low $(^{87}\text{Sr}/^{86}\text{Sr})_i$ and high positive $\epsilon_{\text{Nd}}(t)$ values. The geochemical characteristics described above therefore probably indicate that the Ayishan dacites were derived from the interaction between minor peridotite mantle and melts derived from felsic crustal materials. This is the most reasonable way to generate this kind of magmatic rocks. The relative high $(^{87}\text{Sr}/^{86}\text{Sr})_i$ (0.7108–0.7110) and low $\epsilon_{\text{Nd}}(t)$ values (–6.50 to –6.28) of Ayishan dacites suggest that the proportion of peridotite mantle involved into the mixing process is minor. This possibility is also supported by the high Nb/Ta ratios (17.98–18.53) of the Ayishan dacites, which are significantly greater than those of continental crust.

6.b.2. Natural source of the rhyolites

Several mechanisms have been proposed to interpret the generation of rhyolites: (a) a large mid- to upper-crustal convecting magma body, thermally sustained by underlying mafic sills (e.g. Hildreth, 1981; Lipman, 1984); (b) the silicic magmas, which are derived from partial melting by the injection of basalt into the lower crust on a relatively rapid timescales, rapidly rising through the crust and either intruding intermittently at the surface as rhyolitic subvolcanics (e.g. Huppert & Sparks, 1988); or (c) derivation

from crystal mushes in the shallow crust (e.g. Bachmann & Bergantz, 2004, 2008). Considering the absence of coeval mafic volcanic or intrusive rocks in the South Qilian suture and the mafic microgranular enclaves in these rhyolites, we suggest that the Shihuiyao rhyolites were not significantly influenced by mixing between mafic and silicic magmas. While wall-rock assimilation or magma mixing can easily account for isotopic variations (Ma *et al.* 2015; He *et al.* 2019), the Shihuiyao rhyolites have relatively high $(^{87}\text{Sr}/^{86}\text{Sr})_i = 0.713747$ and low $\epsilon_{\text{Nd}}(t) = -5.48$, consistent with Proterozoic basement rocks in Qilian orogen (Fig. 12). The Shihuiyao rhyolites may therefore be derived from felsic crust with various components at shallow level, which is also supported by the wide-ranging ages of inherited zircon (451–1803 Ma; see Table 1) from these rhyolites and the low MgO and $\text{Fe}_2\text{O}_3^{\text{T}}$ contents. This result is consistent with that shown by the plots of $\text{CaO}/(\text{MgO} + \text{FeO}^{\text{T}} + \text{TiO}_2)$ versus $\text{CaO} + \text{MgO} + \text{FeO}^{\text{T}} + \text{TiO}_2$ (Fig. 11a) and molar $\text{Al}_2\text{O}_3/(\text{MgO} + \text{FeO}^{\text{T}})$ versus $\text{Al}_2\text{O}_3 + \text{MgO} + \text{FeO}^{\text{T}}$ (Fig. 11b), where the samples of Shihuiyao rhyolites are plotted as originating from a greywacke- or metapelitic-dominant source.

6.b.3. Tectonic setting of the lower Silurian subvolcanic rocks

Adakitic rocks derived from the partial melting of continental crust are widely used as a geodynamic indicator of lithospheric delamination, orogenic collapse or crustal thickening in recent studies

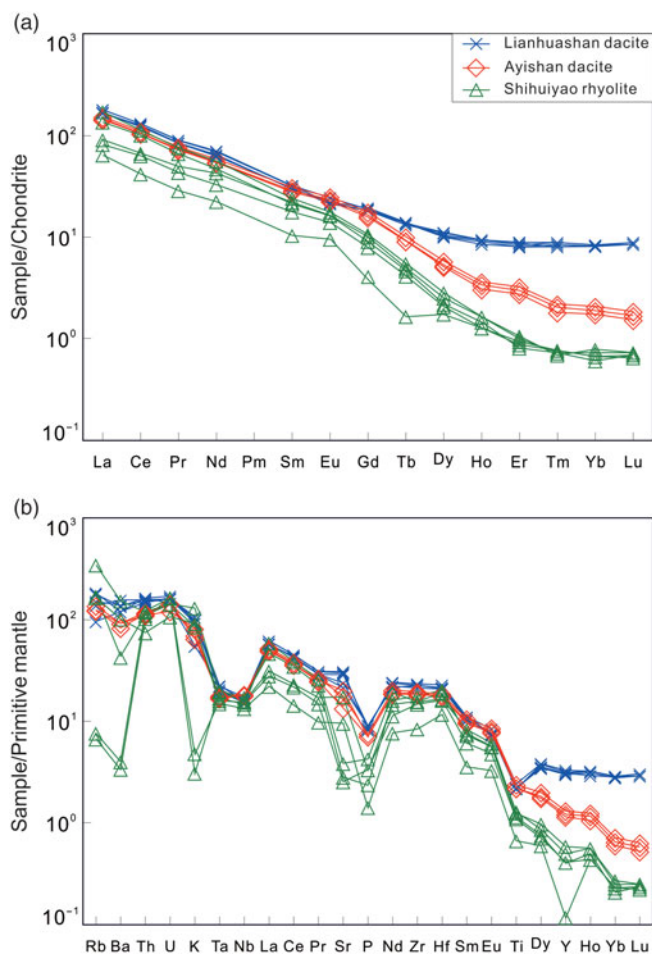


Fig. 7. (Colour online) (a) Plots of chondrite-normalized REE patterns and (b) primitive-mantle-normalized spider diagram for the lower Silurian subvolcanic rocks from the South Qilian suture. Primitive-mantle and chondrite-normalization values are from Sun & McDonough (1989) and Boynton (1984), respectively.

(Castillo, 2012; Ma *et al.* 2015; He *et al.* 2020). Due to the empirical relationships between Sr/Y and La/Yb and crustal thickness in continental collisional orogens (Chapman *et al.* 2015; Hu *et al.* 2017), we use the Sr/Y and La/Yb methods proposed by Hu *et al.* (2017) to calculate the crustal thickness of the Lajishan district at *c.* 433 Ma. The results show that the crustal thickness was over 50 km (see Fig. 13a, b), indicating that adakitic rocks (e.g. Lianhuashan dacites) in this study were derived from partial melting of a thickened crust. The result is consistent with the theory that crustal thickening is common in a continental collision orogeny caused by object extrusion pressure, where deep-seated adakitic melts (derived from > 50 km depth) occur at high pressure (Ma *et al.* 2015; He *et al.* 2020). We therefore suggest that the lower Silurian subvolcanic rocks were derived from a thickened crust. Considering numerous adakitic intrusive rocks with high Sr/Y and the evolutionary history in the Qilian orogen (Li *et al.* 2019b; Yang *et al.* 2020a), we favour a thickened crust model to interpret the occurrence of lower Silurian subvolcanic rocks within the South Qilian suture. According to the high contents of Sr/Y plutons and the calculation of crustal thickness variation, Yang *et al.* (2020a) suggested that the eastern North Qilian experienced clear crustal thickening and thinning during Late Ordovician – late Silurian time, and reached a maximum thickness at *c.* 440 Ma.

Table 3. Whole-rock Sr–Nd isotopic compositions of the lower Silurian subvolcanic rocks of the South Qilian suture

Sample no.	15DG41	15LT2	15LT5	16GK4	16GK6
Rb (ppm)	103	115	94.4	78.2	76.6
Sr (ppm)	198	442	598	416	365
⁸⁷ Rb/ ⁸⁶ Sr	1.507	0.753	0.457	0.544	0.608
⁸⁷ Sr/ ⁸⁶ Sr	0.723044	0.714011	0.711948	0.714186	0.714740
2σ	0.000007	0.000007	0.000006	0.000007	0.000005
(⁸⁷ Sr/ ⁸⁶ Sr) _i	0.7138	0.7094	0.7091	0.7109	0.7110
ε _{Sr} (<i>t</i>)	139.6	76.9	73.4	97.6	99.9
Sm (ppm)	1.55	4.52	4.44	4.30	4.59
Nd (ppm)	10.2	28.6	29.6	25.3	26.9
¹⁴⁷ Sm/ ¹⁴⁴ Nd	0.0919	0.0955	0.0907	0.1030	0.1032
¹⁴³ Nd/ ¹⁴⁴ Nd	0.512060	0.512078	0.512161	0.512040	0.512051
2σ	0.000014	0.000012	0.000012	0.000004	0.000005
(¹⁴³ Nd/ ¹⁴⁴ Nd) _i	0.511801	0.511809	0.511906	0.511750	0.511760
ε _{Nd} (<i>t</i>)	−5.52	−5.37	−3.48	−6.53	−6.32
T _{2DM} (Ma)	1681	1660	1519	1735	1717

*Chondrite uniform reservoir (CHUR) values used are ¹⁴⁷Sm/¹⁴⁴Nd = 0.1967, ¹⁴³Nd/¹⁴⁴Nd = 0.512638; λ_{Sm} = 6.54 × 10^{−11} year^{−1} (Lugmair & Marti, 1978). (¹⁴³Nd/¹⁴⁴Nd)_i and ε_{Nd}(*t*) are calculated considering granitoid age as 433 Ma; single-*T*_{DM} or two-stage (*T*_{2DM}) model age calculation method is from Jahn *et al.* (1999).

Despite the vague collisional timing between the South and Central Qilian blocks, most studies from previous literature suggested that the South Qilian Ocean closed prior to 440 Ma (Huang *et al.* 2015; Yang *et al.* 2015), evidenced by the large number of 470–450-Ma igneous rocks (including volcanic rocks) with continental-arc affinity (Yan *et al.* 2015; Fu *et al.* 2018a; Yang *et al.* 2019a, b) and 450–440-Ma granitoids associated with continental collision (Huang *et al.* 2015; Yang *et al.* 2015; Liu *et al.* 2020) in this district. We therefore suggest that the lower Silurian subvolcanic rocks with ages of *c.* 433 Ma in the South Qilian suture were formed in a post-collisional setting.

6.c. Implications for tectonic transition from Late Ordovician subduction to early Silurian post-collision

Based on their field occurrences, rock assemblages and tectonic affinities, voluminous Middle Ordovician – Silurian igneous rocks are present in the South Qilian suture, and its adjacent blocks are broadly subdivided into three stages: 470–450 Ma, 450–440 Ma and 440–420 Ma (Huang *et al.* 2015; Yang *et al.* 2015; Yan *et al.* 2019b; Sun *et al.* 2020). Numerous diorites and granodiorites with ages of 470–450 Ma intruded into the Cambrian arc-accretionary complex (Fig. 2) and reveal typical subduction-related calc-alkaline geochemical affinity (Niu *et al.* 2016; Yan *et al.* 2019b), implying that a N-facing subduction system and associated Andean-type arc began to develop along the southern part of the central Qilian block during 470–450 Ma (Gehrels *et al.* 2003; Tung *et al.* 2016; Yan *et al.* 2019a). Previous studies suggested that the collision between Qaidam–South Qilian and Central Qilian blocks was in progress during 450–440 Ma (Yang *et al.* 2015; Yan *et al.* 2019a), which is indicated by voluminous I-type granites related to collision within the Central and South Qilian blocks (Tung *et al.* 2016; Yan *et al.* 2015).

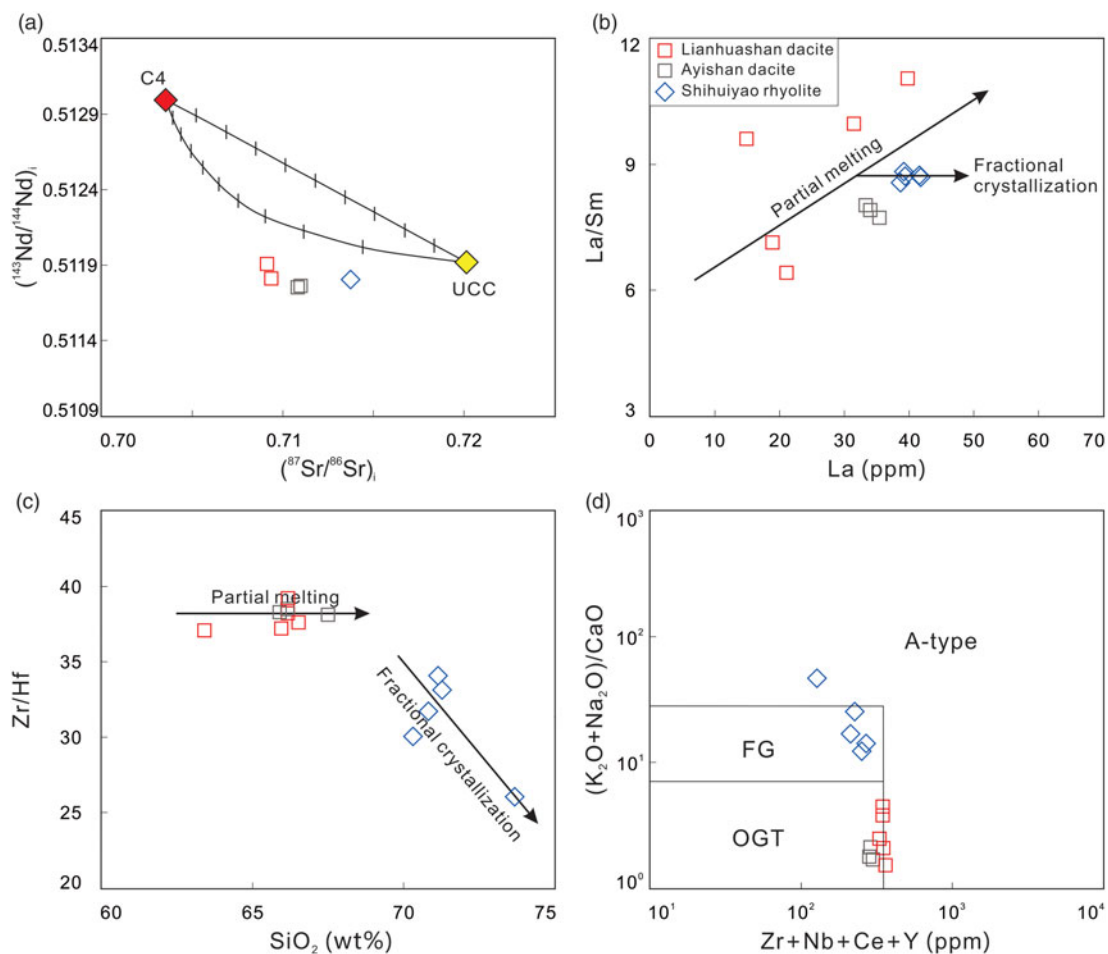


Fig. 8. (Colour online) Plots of (a) $(^{87}\text{Sr}/^{86}\text{Sr})_i$ versus $(^{143}\text{Nd}/^{144}\text{Nd})_i$, (b) La versus La/Sm, (c) SiO_2 versus Zr/Hf and (d) Zr+Nb+Ce+Y versus $(\text{K}_2\text{O}+\text{Na}_2\text{O})/\text{CaO}$ for the lower Silurian subvolcanic rocks from the South Qilian suture. (a) A simple model for classical adakite (represented by C4 from Defant *et al.*, 1992) contaminated/mixed with the upper continental crust (UCC, Jahn *et al.* 1999); no samples fall on the contaminating/mixing curves, indicating that crustal assimilation and fractional crystallization (AFC) did not involve magma evolution of lavas in this study. (b) Partial melting trend for the formation of Lianhuashan dacites. (c) Relatively constant range of Zr/Hf ratio for dacites, probably indicating no intensive fractional crystallization in their evolutionary process. Instead, a decreasing trend with increasing SiO_2 for Shihuiyao rhyolites suggests that the fractional crystallization of zircon played a role in the magmatic stage. (d) Dacites are plotted in the OGT area, whereas Shihuiyao rhyolites are in the FG area in discriminant diagrams after Whalen *et al.* (1987), indicating that Shihuiyao rhyolites experienced obvious fractional crystallization but dacites did not. A – A-type granite; I – I-type granite; S – S-type granite; FG – fractionated felsic granite; OGT – unfractionated M-, I- and S-type granite.

After 440 Ma, the Proto-Tethyan Ocean closed and resulted in early Silurian volcanic activity and magmatic emplacement in the South Qilian suture zone. This process is represented by the voluminous 440–420-Ma post-collisional granitoids, associated high-pressure granulite-facies metamorphism in the South Qilian belt and the Qaidam block, and accompanying anatexis (Yu *et al.* 2014; Yan *et al.* 2015; Zhang *et al.* 2015a; Li *et al.* 2018b). Remarkably, 430-Ma felsic subvolcanic rocks directly intruded into the Upper Ordovician collisional volcanic strata of the Huabaoshan and Yaoshuiquan formations. Systematic field investigation and geochronological studies of the Huabaoshan and Yaoshuiquan formations indicate that they were deposited during Late Ordovician – Silurian time and represent alluvial deposition in a retro-foreland basin in response to collision between the South Qilian and Central Qilian blocks (Yan *et al.* 2019a).

These newly recognized lower Silurian subvolcanic rocks further constrain the upper limit of the Upper Ordovician – Silurian retro-foreland basin, as well as indicate that the regional crust might have undergone post-collisional thickening (as depicted in Fig. 14) after the collision between the Qaidam–South Qilian and Central Qilian

blocks. Available data confirm that early Silurian time was a transition period from collision to post-collision in the South Qilian suture. Here, the collision refers to a stage of continental collision or mountain building, and the post-collision represents exhumation and collapse (Song *et al.* 2015). Generally, collisional magmas are generated by crust during collision and mountain building without involvement of mantle materials; instead, post-collisional magmas are generated in the process of exhumation and collapse with crust–mantle interaction due to mantle upwelling (Prelević *et al.* 2012; Yang *et al.* 2020b). In this study, Silurian subvolcanic rocks were mainly derived from continental crust without involvement of mantle materials. We therefore suggest that these lower Silurian subvolcanic rocks were produced in a transitional stage from collision to post-collision in the South Qilian suture.

7. Conclusions

- (1) Relatively high $(^{87}\text{Sr}/^{86}\text{Sr})_i$ and negative $\epsilon_{\text{Nd}}(t)$ values indicate that the lower Silurian subvolcanic rocks were mainly derived from continental crust. However, significantly different

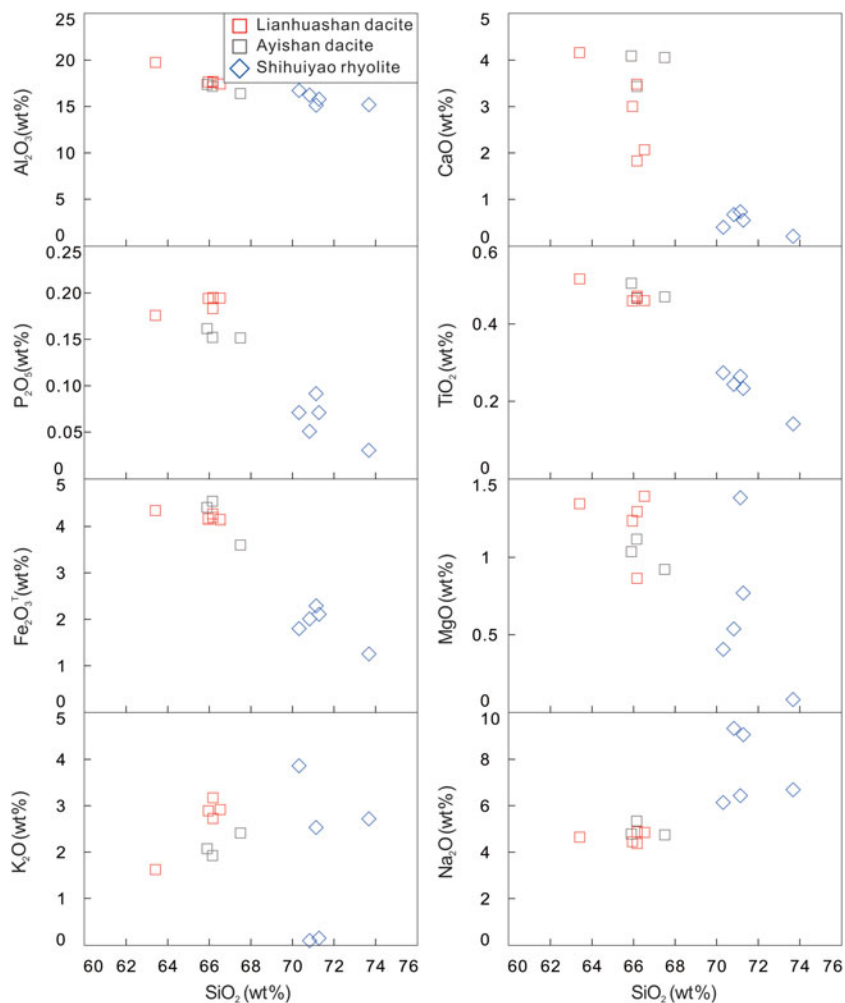


Fig. 9. (Colour online) Harker diagrams of selected major and trace elements for lower Silurian subvolcanic rocks from the South Qilian suture.

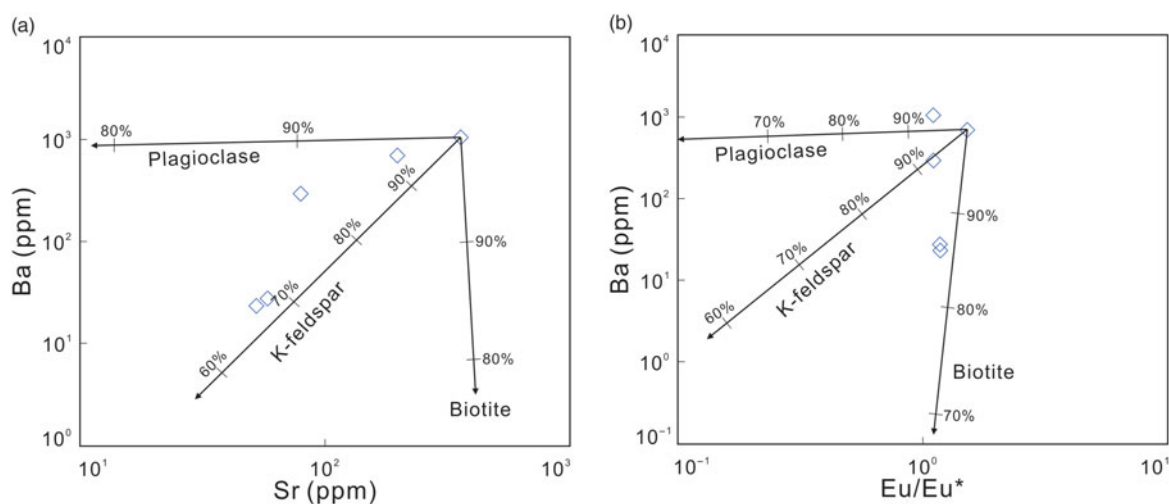


Fig. 10. (Colour online) Plots of (a) Ba versus Sr and (b) Ba versus Eu/Eu^* for Shihuiyao rhyolites from the South Qilian suture. (a) The slow downwards trend along the line of K-feldspar indicates that the fractionation of K-feldspar plays a dominant role in their evolution. (b) The downwards trend indicates the dominance of biotite fractionation in the evolution of the rhyolites. Tick marks indicate the percentage of mineral phases removed (10% intervals). Vectors for K-feldspar, plagioclase and biotite fractionation were calculated using the partition coefficients from Arth (1976).

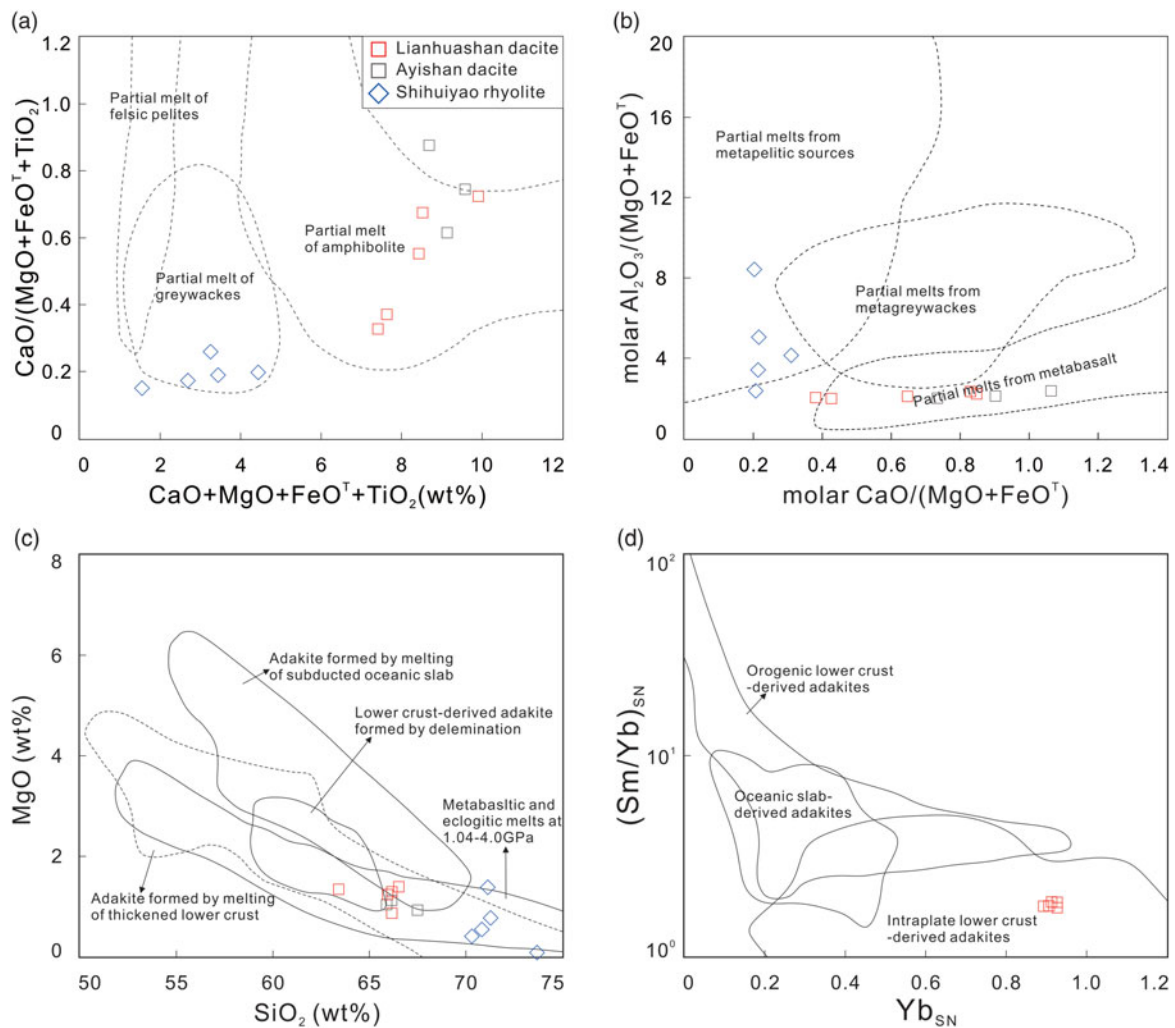


Fig. 11. (Colour online) Plots of (a) $\text{CaO}/(\text{MgO}+\text{FeO}^{\text{T}}+\text{TiO}_2)$ versus $\text{CaO}+\text{MgO}+\text{FeO}^{\text{T}}+\text{TiO}_2$; (b) molar $\text{Al}_2\text{O}_3/(\text{MgO}+\text{FeO}^{\text{T}})$ versus molar $\text{CaO}/(\text{MgO}+\text{FeO}^{\text{T}})$; (c) MgO versus SiO_2 ; and (d) $(\text{Sm}/\text{Yb})_{\text{SN}}$ versus Yb_{SN} for the lower Silurian subvolcanic rocks from the South Qilian suture. (a, b) Fields from Douce & Harris (1998), Sylvester (1998), Douce (1999) and Altherr *et al.* (2000). (c) Data for metabasaltic and eclogite experimental melts (1–4.0 GPa) are from Rapp & Watson (1995); the fields for subducted oceanic crust-derived adakites, delaminated or thickened lower crust-derived adakitic rocks are from Wang *et al.* (2006). (d) Source-normalized (SN) data, normalized to mafic lower continental crust with $\text{Yb} = 1.5$ ppm and $\text{Sm}/\text{Yb} = 1.87$ for continental adakite (after Ma *et al.* 2015).

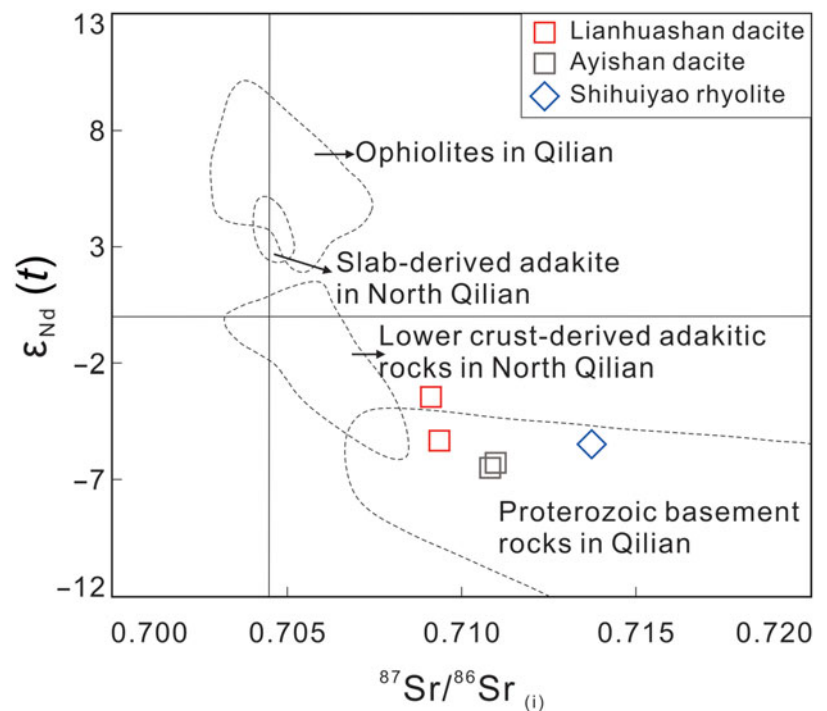


Fig. 12. (Colour online) Plots of $\epsilon_{\text{Nd}}(t = 433 \text{ Ma})$ versus $(^{87}\text{Sr}/^{86}\text{Sr})_i$ for the lower Silurian subvolcanic rocks from the South Qilian suture. These rocks have Sr–Nd isotopic compositions distinct from slab-derived adakites in North Qilian (after Chen *et al.* 2012) and lower crust-derived adakitic rocks (after Zhang *et al.* 2006b; Tseng *et al.* 2009; Zhang *et al.* 2017a; Li *et al.* 2019b; Yang *et al.* 2020a), but similar to intrusive rocks derived from Proterozoic basement (after Zhang *et al.* 2006a, b; Tung *et al.* 2016) in the Qilian Orogen, indicating that they are derived from continental crust. Data describing ophiolite in Qilian are from Hou *et al.* (2006a, b) and Fu *et al.* (2018a).

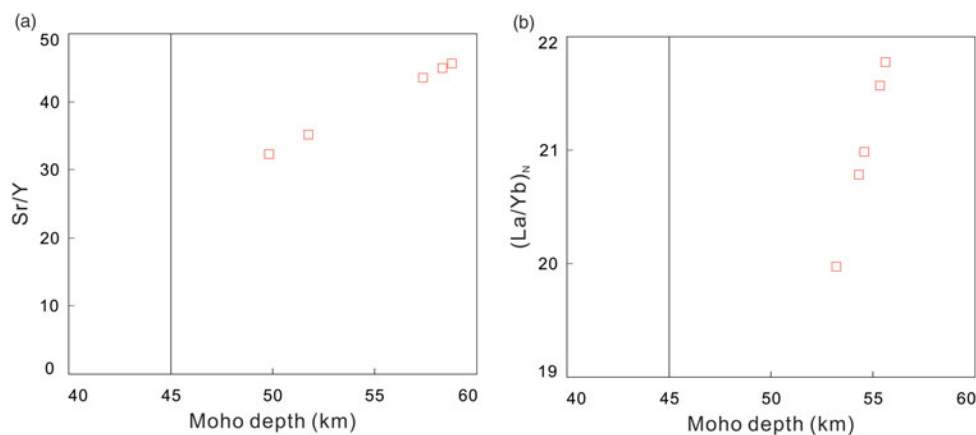


Fig. 13. (Colour online) Plots of Moho depth versus (a) Sr/Y and (b) $(La/Yb)_N$ for adakitic rocks of the Lianhuashan dacites. The calculation methods are after Hu *et al.* (2017), and the results reveal that the crustal thickness was over 50 km.

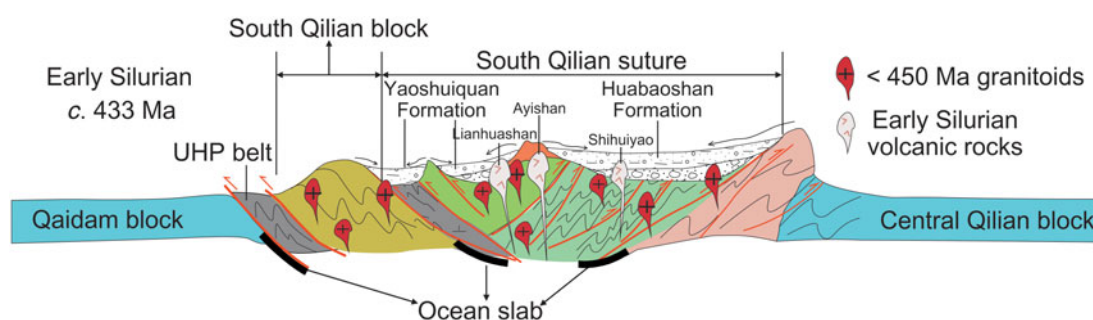


Fig. 14. Schematic tectonic model for the southern part of the Qilian Orogen during early Silurian time.

patterns of REEs and spider diagrams probably imply they have distinctly generation mechanisms with or without extensive fractional crystallization.

- (2) The modelling calculation of Sr/Y and La/Yb and geochemical data indicate that the lower Silurian subvolcanic rocks from the South Qilian suture were derived from partial melting of a thickened crust in a post-collision setting.
- (3) Considering the tectonic evolution and regional geology, we suggest that the early Silurian period was a transitional time from collision to post-collision for the South Qilian suture zone.

Acknowledgments. This study was supported by the National Natural Science Foundation of China (42072266, 41872241, 41702239, 41672221), China Geological Survey (DD20190006) and the Bureau of Geological Exploration and Development of Qinghai Province (2019-45). The authors thank two reviewers and editor Kathryn Goodenough for their valuable suggestions.

References

Adam J and Green T (2006) Trace element partitioning between mica- and amphibole-bearing garnet lherzolite and hydrous basanitic melt: 1. Experimental results and the investigation of controls on partitioning behaviour. *Contributions to Mineralogy and Petrology* **152**, 1–17.

Altherr R, Holl A, Hegner E, Langer C and Kreuzer H (2000) High-potassium, calc-alkaline I-type plutonism in the European Variscides: Northern Vosges (France) and northern Schwarzwald (Germany). *Lithos* **50**, 51–73.

Annen C, Blundy JD and Sparks RSJ (2006) The genesis of intermediate and silicic magmas in deep crustal hot zones. *Journal of Petrology* **3**, 505–39.

Arth J (1976) Behavior of trace elements during magmatic processes—a summary of theoretical models and their applications. *Journal of Research of the U. S. Geological Survey* **4**, 41–7.

Bachmann O and Bergantz GW (2004) On the origin of crystal-poor rhyolites: extracted from batholithic crystal mushes. *Journal of Petrology* **45**, 1565–82.

Bachmann O and Bergantz GW (2008) The magma reservoirs that feed super-eruptions. *Elements* **4**, 17–21.

Belousova EA, Griffin WL, Reilly SYO and Fisher NI (2002) Igneous zircon: trace element composition as an indicator of source rock type. *Contributions to Mineralogy and Petrology* **143**, 602–22.

Boynton WV (1984) Geochemistry of the rare earth elements: Meteorite studies. In *Rare Earth Element Geochemistry* (ed. P Henderson), pp. 63–114. New York, NY, USA: Elsevier.

Castillo PR (2006) An overview of adakite petrogenesis. *Chinese Science Bulletin* **51**, 258–68.

Castillo PR (2012) Adakite petrogenesis. *Lithos* **134**, 304–16.

Castillo PR, Janney PE and Solidum RU (1999) Petrology and geochemistry of Camiguin Island, southern Philippines: insights to the source of adakites and other lavas in a complex arc setting. *Contributions to Mineralogy and Petrology* **134**, 33–51.

Chapman JB, Ducea MN, DeCelles PG and Profeta L (2015) Tracking changes in crustal thickness during orogenic evolution with Sr/Y: an example from the North American Cordillera. *Geology* **43**, 919–22.

Chen B, Jahn BM and Suzuki K (2013) Petrological and Nd–Sr–Os isotopic constraints on the origin of high-Mg adakitic rocks from the North China Craton: tectonic implications. *Geology* **41**, 91–4.

Chen YX, Xia XH and Song SG (2012) Petrogenesis of Aoyougou high-silica adakite in the North Qilian orogen, NW China: evidence for decompression melting of oceanic slab. *Chinese Science Bulletin* **57**, 2289–301.

Cui JW, Tian LM, Sun JY and Yang C (2019) Geochronology and geochemistry of early Palaeozoic intrusive rocks in the Lajishan area of the eastern south Qilian Belt, Tibetan Plateau: implications for the tectonic evolution of South Qilian. *Geological Journal* **54**, 3404–20.

Defant MJ and Drummond MS (1990) Derivation of some modern arc magmas by melting of young subducted lithosphere. *Nature* **347**, 662–5.

- Defant MJ, Jackson TE, Drummond MS, De Boer JZ, Bellon H, Feigenson MD, Maury RC, Stewart RH and Cawood P (1992) The geochemistry of young volcanism throughout western Panama and southeastern Costa Rica: an overview. *Journal of the Geological Society, London*, **149**, 569–79.
- DePaolo DJ (1981) A neodymium and strontium isotopic study of the Mesozoic calcalkaline granitic batholiths of the Sierra Nevada and Peninsular Ranges, California. *Journal of Geophysical Research* **86**, 10470–88.
- Douce AEP (1999) What do experiments tell us about the relative contributions of crust and mantle to the origin of granitic magmas? In *Understanding Granites: Integrating New and Classical Techniques* (eds A Castro, C Fernández and JL Vigneresse), pp. 55–75. Geological Society of London, Special Publication no. 168.
- Douce AEP and Harris N (1998) Experimental constraints on Himalayan anatexis. *Journal of Petrology* **39**, 689–710.
- Dungan MA and Davidson J (2004) Partial assimilative recycling of the mafic plutonic roots of arc volcanoes: an example from the Chilean Andes. *Geology* **32**, 773–6.
- Fu CL, Yan Z, Guo XQ, Niu M L, Xia WJ, Wang ZQ and Li JL (2014) Geochemistry and SHRIMP zircon U–Pb age of diabases in the Lajishankou ophiolitic mélange, South Qilian terrane. *Acta Petrologica Sinica* **30**, 1695–706.
- Fu CL, Yan Z, Jonathan CA, Guo XQ and Xiao WJ (2019a) Abyssal and supra-subduction peridotites in the Lajishan Ophiolite Belt: implication for initial subduction of the Proto-Tethyan Ocean. *The Journal of Geology* **127**, 393–410.
- Fu CL, Yan Z, Jonathan CA, Xiao WJ, Buckman S, Wang BZ, Li WF, Li YS and Ren HD (2020) Multiple subduction processes of the Proto-Tethyan Ocean: implication from Cambrian intrusions along the North Qilian suture zone. *Gondwana Research* **87**, 207–23.
- Fu CL, Yan Z, Wang ZQ, Buckman S, Aitchison JC, Niu ML, Cao B, Guo XQ, Li XC, Li YS and Li JL (2018a) Lajishankou ophiolite complex: implications for Paleozoic multiple accretionary and collisional events in the South Qilian belt. *Tectonics* **37**, 1321–46.
- Fu CL, Yan Z, Wang ZQ, Niu ML, Guo XQ, Yu LJ and Li JL (2018b) Texture and composition of the Lajishankou accretionary wedge of the South Qilian belt, NW China. *Acta Petrologica Sinica* **34**, 2049–64 (in Chinese with English abstract).
- Fu CL, Zhen Y, Guo XQ, Niu ML, Cao B, Wu Q, Li XC and Wang ZQ (2019b) Assembly and dispersal history of continental blocks within the Altun-Qilian-North Qaidam mountain belt, NW China. *International Geology Review* **61**(4), 424–47.
- Fu D, Kusky TM, Wilde SA, Polat A, Huang B and Zhou ZP (2018c) Early Paleozoic collision-related magmatism in the eastern North Qilian orogen, northern Tibet: a linkage between accretionary and collisional orogenesis. *Geological Society of America Bulletin* **131**, 1031–56.
- Gao YY, Li XH, Griffin WL, O'Reilly SY and Wang YF (2014) Screening criteria for reliable U–Pb geochronology and oxygen isotope analysis in uranium-rich zircons: a case study from the Suzhou A-type granites, SE China. *Lithos* **192**, 180–91.
- Gehrels GE, Kapp P, DeCelles P, Pullen A, Blakey R, Weislogel A, Ding L, Guynn J, Martin A, McQuarrie N and Yin A (2011) Detrital zircon geochronology of pre-Tertiary strata in the Tibetan-Himalayan orogen. *Tectonics* **30**, 10–1029.
- Gehrels GE, Yin A and Wang X (2003) Magmatic history of the northeastern Tibetan Plateau. *Journal of Geophysical Research*, **108**, 2423.
- Gertisser R and Keller J (2000) From basalt to dacite: origin and evolution of the calc-alkaline series of Salina, Aeolian Arc, Italy. *Contributions to Mineralogy and Petrology* **139**, 607–26.
- Grove TL, Elkins-Tanton LT, Parman SW, Chatterjee N, Müntener O and Gaetani GA (2003) Fractional crystallization and mantle-melting controls on calc-alkaline differentiation trends. *Contributions to Mineralogy and Petrology* **145**, 515–33.
- Guo ZP, Li WY, Zhang ZW, Gao YB, Li K, Kong HL and Qian B (2015) Petrogenesis of Lumanshan granites in Hualong area of southern Qilian Mountain: constraints from geochemistry, zircon U–Pb geochronology and Hf isotope. *Geology in China* **42**, 864–80 (in Chinese with English abstract).
- Hawkesworth CJ, Gallagher K, Hergt JM and McDermott F (1993) Mantle and slab contributions in arc magmas. *Annual Review of Earth and Planetary Sciences* **21**, 175–204.
- He XH, Tan SC, Liu Z, Bai ZJ, Wang XC, Wang YC and Zhong H (2020) Petrogenesis of the Early Cretaceous Aolunhua adakitic monzogranite porphyries, southern Great Xing'an Range, NE China: implication for geodynamic setting of Mo mineralization. *Minerals* **10**, 332.
- He XH, Zhou RJ, Tan SC, Liu Z, Wang GC, Jiang ZQ and Cao Y (2019) Late Cretaceous–Eocene magmatism induced by slab rollback and breakoff in the Tengchong terrane, SW China. *International Geology Review*, published online 31 December 2019, <https://doi.org/10.1080/00206814.2019.1709567>.
- Hildreth W (1981) Gradients in silicic magma chambers: implications for lithospheric magmatism. *Journal of Geophysical Research: Solid Earth* **86**, 10153–92.
- Hofmann AW (1997) Mantle geochemistry: the message from oceanic volcanism. *Nature* **385**, 219–29.
- Hou QY, Zhao ZD, Zhang HF, Zhang BR and Chen YL (2006a) Indian Ocean–MORB-type isotopic signature of Yushigou ophiolite in north Qilian Mountains and its implications. *Science in China Series D–Earth Sciences* **49**, 561–72.
- Hou QY, Zhao ZD, Zhang HF, Zhang BR, Zhang L and Chen YL (2006b) Discussion on the tectonic affinity of ancient oceanic mantle in Western Qinling–Songpan continental tectonic node, China: from elemental and Sr–Nd–Pb isotopic evidences. *Acta Petrologica Sinica* **22**, 2901–9 (in Chinese with English abstract).
- Hou ZQ, Gao YF, Qu XM, Rui ZY and Mo XX (2004) Origin of adakitic intrusives generated during mid-Miocene east–west extension in southern Tibet. *Earth and Planetary Science Letters* **220**, 139–55.
- Hu FY, Ducea MN, Liu SW and Chapman JB (2017) Quantifying crustal thickness in continental collisional belts: global perspective and a geologic application. *Scientific Reports* **7**, 7058.
- Huang H, Niu YL, Nowell G, Zhao ZD, Yu XH and Mo XX (2015) The nature and history of the Qilian Block in the context of the development of the Greater Tibetan Plateau. *Gondwana Research* **28**, 209–24.
- Huppert HE and Sparks RSJ (1988) The generation of granitic magmas by intrusion of basalt into continental crust. *Journal of Petrology* **29**, 599–624.
- Jahn BM, Wu FY, Lo CH and Tsai CH (1999) Crust–mantle interaction induced by deep subduction of the continental crust: geochemical and Sr–Nd isotopic evidence from post-collisional mafic–ultramafic intrusions of the northern Dabie complex, central China. *Chemical Geology* **157**, 119–46.
- Kay SM, Godoy E and Kurtz A (2005) Episodic arc migration, crustal thickening, subduction erosion, and magmatism in the south-central Andes. *Geological Society of America Bulletin* **117**, 67–88.
- Li CF, Li XH, Li QL, Guo JH and Yang YH (2012) Rapid and precise determination of Sr and Nd isotopic ratios in geological samples from the same filament loading by thermal ionization mass spectrometry employing a single-step separation scheme. *Analytica Chimica Acta* **727**, 54–60.
- Li M, Wang C, Li RS, Meert JG, Peng Y and Zhang JH (2019a) Identifying late Neoproterozoic–early Paleozoic sediments in the South Qilian Belt, China: a peri-Gondwana connection in the northern Tibetan Plateau. *Gondwana Research* **76**, 173–84.
- Li SZ, Zhao SJ, Liu X, Cao HH, Yu S, Li XY, Somerville I, Yu SY and Suo YH (2018a) Closure of the Proto-Tethys Ocean and Early Paleozoic amalgamation of microcontinental blocks in East Asia. *Earth-Science Reviews* **186**, 37–75.
- Li XH, Liu Y, Li QL, Guo CH and Chamberlain KR (2009) Precise determination of Phanerozoic zircon Pb/Pb age by multicollector SIMS without external standardization. *Geochemistry, Geophysics, Geosystems* **10**, Q06011.
- Li XY, Li SZ, Yu SY, Santosh M, Zhao SJ, Guo XY, Cao HH, Wang YM and Huang ZB (2018b) Early Paleozoic arc–back–arc system in the southeastern margin of the North Qilian Orogen, China: constraints from geochronology, and whole-rock elemental and Sr–Nd–Pb–Hf isotopic geochemistry of volcanic suites. *Gondwana Research* **59**, 9–26.
- Li YL, Tong X, Zhu YH, Lin JW, Zheng JP and Brouwer FM (2018c) Tectonic affinity and evolution of the Precambrian Qilian block: insights from petrology, geochemistry and geochronology of the Hualong Group in the Qilian Orogen, NW China. *Precambrian Research* **315**, 179–200.
- Li YL, Xiao WJ, Li ZY, Wang K, Zheng JP and Brouwer FM (2020) Early Neoproterozoic magmatism in the Central Qilian block, NW China: geochronological and petrogenetic constraints for Rodinia assembly. *Geological Society of America Bulletin* **132**(11–12), 2145–31, doi: [10.1130/B35637.1](https://doi.org/10.1130/B35637.1).

- Liu YS, Xu LJ, Yu SY, Zhang JX, Guo J, Peng YB and Zhou GS (2019b) Partial melting of thickened lower crust in post-collisional setting: evidence from high silicon adakitic granites in the North Qilian orogeny. *Geological Journal* **55**, 3990–4007.
- Liang Q, Jing H and Gregoire DC (2000) Determination of trace elements in granites by inductively coupled plasma mass spectrometry. *Talanta* **51**, 507–13.
- Lipman PW (1984) The roots of ash flow calderas in western North America: windows into the tops of granitic batholiths. *Journal of Geophysical Research: Solid Earth* **89**, 8801–41.
- Liu XT, Li BK, Han JL, Ren EF, Gao DL, Du YS, Ren QH and Zhang Y (2020) Geochemistry and zircon U–Pb geochronology of the Early Palaeozoic S-type granites in the eastern Qilian block, Northwest China. *Acta Geologica Sinica (English Edition)*, published online 13 February 2020, doi: [10.1111/1755-6724.14504](https://doi.org/10.1111/1755-6724.14504).
- Liu YS, Hu ZC, Zong KQ, Gao CG, Gao S, Xu J and Chen HH (2010) Reappraisal and refinement of zircon U–Pb isotope and trace element analyses by LA–ICP–MS. *Chinese Science Bulletin* **55**, 1535–46.
- Liu YS, Zong KQ, Kelemen PB and Gao S (2008) Geochemistry and magmatic history of eclogites and ultramafic rocks from the Chinese continental scientific drill hole: subduction and ultrahigh-pressure metamorphism of lower crustal cumulates. *Chemical Geology* **247**, 133–53.
- Ludwig KR (2001) *User Manual for Isoplot/Ex rev. 2.49*. Berkeley: Berkeley Geochronology Centre, Special Publication no. 1a, pp. 56.
- Lugmair GW and Marti K (1978) Lunar initial $^{143}\text{Nd}/^{144}\text{Nd}$: differential evolution of the lunar crust and mantle. *Earth and Planetary Science Letters* **39**, 349–57.
- Ma Q, Zheng JP, Xu YG, Griffin WL and Zhang RS (2015) Are continental “adakites” derived from thickened or foundered lower crust? *Earth and Planetary Science Letters* **419**, 125–33.
- Ma W, Jia JT, Li WF, Ma YJ, Lei XQ, Ren EF and Xu B (2017) LA–ICP–MS zircon U–Pb age of gabbro from Yangkang area in South Qilian and its geological significance. *Northwestern Geology* **50**, 74–82 (in Chinese with English abstract).
- Martin H, Smithies RH, Rapp R, Moyen JF and Champion D (2005) An overview of adakite, tonalite–trondhjemite–granodiorite (TTG), and sanukitoid: relationships and some implications for crustal evolution. *Lithos* **79**, 1–24.
- Niu GZ, Huang G, Deng CS, Xu Y, Chen T, Ji C and Li WJ (2016) LA–ICP–MS zircon U–Pb ages of metamorphic volcanic rocks in Balonggongge'er Formation of South Qilian Mountain in Qinghai Province and their geological significance. *Geological Bulletin of China*, **35**, 1441–7 (in Chinese with English abstract).
- Prelević D, Akal C, Foley SF, Romer RL, Stracke A and Van Den Bogaard P (2012) Ultrapotassic mafic rocks as geochemical proxies for post-collisional dynamics of orogenic lithospheric mantle: the case of southwestern Anatolia, Turkey. *Journal of Petrology* **53**, 1019–55.
- Qian Q and Hermann J (2013) Partial melting of lower crust at 10–15 kbar: constraints on adakite and TTG formation. *Contributions to Mineralogy and Petrology* **165**, 1195–224.
- Qian Q, Zhang Q and Sun XM (2001) Tectonic setting and mantle source characteristics of Jiugequan basalts, North Qilian: constraints from trace elements and Nd–Isotopes. *Acta Petrologica Sinica* **17**, 385–94 (in Chinese with English abstract).
- Qiu JX, Zeng GC, Wang SY and Zhu YH (1995) Early Palaeozoic volcanic rocks in Laji Mountain orogenic belt, Qinghai province. *Northwest Geoscience*, **16**, 69–83 (in Chinese with English abstract).
- Rapp RP and Watson EB (1995) Dehydration melting of metabasalt at 8–32 kbar: implications for continental growth and crust–mantle recycling. *Journal of Petrology* **36**, 891–931.
- Rodriguez C, Selles D, Dungan M, Langmuir C and Leeman W (2007) Adakitic dacites formed by intracrustal crystal fractionation of water-rich parent magmas at Nevado de Longav volcano (36.2 degrees S; Andean Southern Volcanic Zone, central Chile). *Journal of Petrology* **48**, 2033–61.
- Song SG, Niu YL, Li S and Xia XH (2013) Tectonics of the North Qilian orogen, NW China. *Gondwana Research* **23**, 1378–401.
- Song SG, Niu YL, Su L, Zhang C and Zhang L (2014) Continental orogenesis from ocean subduction, continent collision/subduction, to orogen collapse, and orogen recycling: the example of the North Qaidam UHPM belt, NW China. *Earth-Science Reviews* **129**, 59–84.
- Song SG, Wang MJ, Wang C and Niu YL (2015) Magmatism during continental collision, subduction, exhumation and mountain collapse in collisional orogenic belts and continental net growth: a perspective. *Science China Earth Sciences* **58**, 1284–304.
- Stacey JS and Kramers JD (1975) Approximation of terrestrial lead isotope evolution by a two-stage model. *Earth and Planetary Science Letters* **26**, 207–21.
- Sun SS and McDonough WF (1989) Chemical and isotopic systematics of oceanic basalts: implications for mantle composition and processes. In *Magmatism in the Ocean Basins* (eds AD Saunders and MJ Norry), pp. 313–45. Geological Society of London, Special Publication no. 42.
- Sun Y, Niu ML, Li XC, Wu Q, Cai QR, Yuan XY and Li C (2020) Petrogenesis and tectonic implications from the Ayishan Group in the South Qilian Belt, NW China. *Geological Journal*, published online 23 April 2020, <https://doi.org/10.1002/gj.3851>.
- Sun Y, Niu ML, Li XC, Wu Q, Cai QR, Yuan XY, Wen FL and Li C (2019) Geochemical characteristics and geochronology of the rhyolites from Ayishan Group in the Lajishan area and its tectonic significance. *Chinese Journal of Geology* **54**, 1016–30 (in Chinese with English abstract).
- Sylvester PL (1998) Post-collisional strongly peraluminous granites. *Lithos* **45**, 29–44.
- Tanaka T, Togashi S, Kamioka H, Amakawa H, Kagami H, Hamamoto T, Yuhara M, Orihashi Y, Yoneda S, Shimizu H, Kunimaru T, Takahashi K, Yanagi T, Nakano T, Fujimaki H, Shinjo R, Asahara Y, Tanimizu M and Dragusanu C (2000) JNdi-1: a neodymium isotopic reference in consistency with LaJolla neodymium. *Chemical Geology* **168**, 279–81.
- Tsang CY, Yang HJ, Yang HY, Liu DY, Wu CL, Cheng CK, Chen CH and Ker CM (2009) Continuity of the North Qilian and North Qinling orogenic belts, Central Orogenic System of China: evidence from newly discovered Palaeozoic adakitic rocks. *Gondwana Research* **16**, 285–93.
- Tung KA, Yang HY, Liu DY, Zhang JX, Yang HJ, Shau YH and Tsang CY (2012) The amphibolite facies metamorphosed mafic rocks from the Maxianshan area, Qilian block, NW China: a record of early Neoproterozoic arc magmatism. *Journal of Asian Earth Sciences* **46**, 177–89.
- Tung KA, Yang HY, Yang HJ, Smith A, Liu DY, Zhang JX, Wu CL, Shau YH, Wen DJ and Tsang CY (2016) Magma sources and petrogenesis of the Early–Middle Palaeozoic backarc granitoids from the central part of the Qilian Block, NW China. *Gondwana Research* **38**, 197–219.
- Wan YS, Xu ZQ, Yang JS and Zhang JX (2003) The Precambrian high-grade basement of the Qilian terrane and neighboring areas: its ages and compositions. *Acta Geoscientia Sinica* **24**, 319–24 (in Chinese with English abstract).
- Wan YS, Zhang JX, Yang JS and Xu ZQ (2006) Geochemistry of high-grade metamorphic rocks of the North Qaidam mountains and their geological significance. *Journal of Asian Earth Sciences* **28**, 174–84.
- Wang C, Li RS, Smithies RH, Li M, Peng Y, Chen FN and He SP (2017) Early Palaeozoic felsic magmatic evolution of the western Central Qilian belt, Northwestern China, and constraints on convergent margin processes. *Gondwana Research* **41**, 301–24.
- Wang DS, Wang T, Yan J and Lin X (2018a) Petrogenesis and tectonic implications of early Palaeozoic igneous rocks of the western South Qilian Belt, central China. *International Geology Review* **60**, 844–64.
- Wang Q and Liu XY (1976) Paleo-Oceanic crust of the Chilienshan region, western China and its tectonic significance. *Scientia Geologica Sinica* **11**, 42–55 (in Chinese with English abstract).
- Wang Q, Xu JF, Jian P, Bao ZW, Zhao ZH, Li CF, Xiong XL and Ma JL (2006) Petrogenesis of adakitic porphyries in an extensional tectonic setting, Dexing, South China: implications for the genesis of porphyry copper mineralization. *Journal of Petrology* **47**, 119–44.
- Wang T, Wang DS, Wang ZQ, Lu HF, Wang MQ and Santosh M (2018b) Geochemical and geochronological study of early Palaeozoic volcanic rocks from the Lajishan accretionary complex, NW China: petrogenesis and tectonic implications. *Lithos* **314–315**, 323–36.
- Wanless VD, Perfit MR, Ridley WI and Klein E (2010) Dacite petrogenesis on Mid-Ocean ridges: evidence for oceanic crustal melting and assimilation. *Journal of Petrology* **51**, 2377–410.

- Wedepohl KH (1995) The composition of the continental crust. *Geochimica et Cosmochimica Acta* **59**, 1217–32.
- Weis D, Kieffer B, Maerschalk C, Barling J, de Jong J, Williams GA, Hanano D, Pretorius W, Mattielli N, Scoates JS, Goolaerts A, Friedman RM and Mahoney JB (2006) High-precision isotopic characterization of USGS reference materials by TIMS and MC-ICP-MS. *Geochemistry, Geophysics, Geosystems* **7**, Q08006.
- Whalen JB, Currie KL and Chappell BW (1987) A-type granite: geochemical characteristics, discrimination and petrogenesis. *Contributions to Mineralogy and Petrology* **95**, 407–19.
- White LT and Ireland TR (2012) High-Uranium matrix effect in zircon and its implications for SHRIMP U–Pb age determinations. *Chemical Geology* **306**, 78–91.
- Wu CL, Xu XY, Gao QM, Li XM, Lei M, Gao YH, Frost RB and Wooden JL (2010) Early Palaeozoic granitoid magmatism and tectonic evolution in North Qilian, NW China. *Acta Petrologica Sinica* **26**, 1027–44.
- Wu CL, Yang JS, Yang HY, Wooden J, Shi RD, Chen SY and Zheng QG (2004) Dating of two types of granite from north Qilian, China. *Acta Petrologica Sinica* **20**, 425–32 (in Chinese with English abstract).
- Xia LQ, Li XM, Yu JY and Wang GQ (2016) Mid-Late Neoproterozoic to early Paleozoic volcanism and tectonic evolution of the Qilianshan, NW China. *GeoResJ* **9–12**, 1–41.
- Xiao WJ, Windley BF, Yong Y, Yan Z, Yuan C, Liu CZ and Li JL (2009) Early Paleozoic to Devonian multiple-accretionary model for the Qilian Shan, NW China. *Journal of Asian Earth Sciences* **35**, 323–33.
- Xu JF, Shinjo R, Defant MJ, Wang Q and Rapp RP (2002) Origin of Mesozoic adakitic intrusive rocks in the Ningzhen area of east China: partial melting of delaminated lower continental crust? *Geology* **30**, 1111–4.
- Xu ZQ, Xu HF, Zhang JX, Li HB, Zhu ZZ, Qu JJ, Chen DZ, Chen JL and Yang KC (1994) The Zhoulangnanshan Caledonian subductive complex in the Northern Qilian Mountains and its dynamics. *Acta Geologica Sinica* **68**, 1–15 (in Chinese with English abstract).
- Yan Z, Aitchison J, Fu CL, Guo XQ, Niu ML, Xia WJ and Li JL (2015) Hualong Complex, South Qilian terrane: U–Pb and Lu–Hf constraints on Neoproterozoic micro-continental fragments accreted to the northern Proto-Tethyan margin. *Precambrian Research* **266**, 65–85.
- Yan Z, Fu CL, Aitchison J, Buckman S, Niu ML, Cao B, Sun Y, Guo XQ, Wang ZQ and Zhou RJ (2019a) Retro-foreland basin development in response to Proto-Tethyan Ocean closure, NE Tibet Plateau. *Tectonics* **38**, 4229–48.
- Yan Z, Fu CL, Aitchison J, Niu ML, Buckman S and Cao B (2019b) Early Cambrian Muli arc–ophiolite complex: a relic of the Proto-Tethys oceanic lithosphere in the Qilian Orogen, NW China. *International Journal of Earth Sciences* **108**, 1147–64.
- Yan Z, Fu CL, Aitchison JC, Zhou RJ, Buckman S and Chen L (2020) Silurian sedimentation in the South Qilian Belt: arc–continent collision-related deposition in the NE Tibet Plateau? *Acta Geologica Sinica* **94**(4), 901–13.
- Yan Z, Xiao WJ, Wang ZQ and Li JL (2007) Integrated analyses constraining the provenance of sandstones, mudstones and conglomerates, a case study: the Laojunshan conglomerate, Qilian orogen, northwest China. *Canadian Journal of Earth Sciences* **44**, 961–86.
- Yan Z, Xiao WJ, Windley BF, Wang ZQ and Li JL (2010) Silurian clastic sediments in the North Qilian Shan, NW China: chemical and isotopic constraints on their forearc provenance with implications for the Paleozoic evolution of the Tibetan Plateau. *Sedimentary Geology* **231**, 98–114.
- Yang H, Zhang HF, Luo BJ, Zhang J, Xiong ZL, Gao L and Pan FB (2015) Early Paleozoic intrusive rocks from the eastern Qilian orogen, NE Tibetan Plateau: petrogenesis and tectonic significance. *Lithos* **224–225**, 13–31.
- Yang H, Zhang HF, Xiao WJ, Luo BJ, Gao Z, Lu T, Zhang LQ and Guo L (2020a) Petrogenesis of Early Paleozoic high Sr/Y intrusive rocks from the North Qilian orogen: implication for diachronous continental collision. *Lithosphere* **12**, 53–73.
- Yang JH, Du YS, Cawood PA and Xu YJ (2012) From subduction to collision in the northern Tibetan Plateau: evidence from the Early Silurian clastic rocks, Northwestern China. *The Journal of Geology* **120**, 49–67.
- Yang LM, Song SG, Su L, Allen MB, Niu YL, Zhang GB and Zhang YQ (2019a) Heterogeneous oceanic arc volcanic rocks in the South Qilian accretionary belt (Qilian Orogen, NW China). *Journal of Petrology* **60**, 85–116.
- Yang LM, Su L, Song SG, Allen MB, Bi HZ, Feng D, Li WF and Li YG (2019b) Interaction between oceanic slab and metasomatized mantle wedge: constraints from sodic lavas from the Qilian Orogen, NW China. *Lithos* **348–349**, 105182.
- Yang SX, Su L, Song SG, Mark BA, Feng D, Wang MJ, Wang C and Zhang HY (2020b) Melting of subducted continental crust during collision and exhumation: insights from granitic rocks from the North Qaidam UHP metamorphic belt, NW China. *Lithos* **378–379**, 105794.
- Yang WR, Deng QL and Wu XL (2002) Major characteristics of the Lajishan orogenic belt of the South Qilian Mountains and its geotectonic attribute. *Acta Geologica Sinica* **76**, 110–7 (in Chinese with English abstract).
- Yu S, Zhang Z, Mattinson CG, del Real PG, Li Y and Gong J (2014) Paleozoic HP granulite–facies metamorphism and anatexis in the Dulan area of the North Qaidam UHP terrane, western China: constraints from petrology, zircon U–Pb and amphibole Ar–Ar geochronology. *Lithos*, **198–199**, 58–76.
- Zhang HF, Jin LL, Zhang L, Yuan HL, Zhou L and Zhang BR (2006a) Pb and Nd isotopic compositions of basement and granitoid in the Qilianshan: constraints on tectonic affinity. *Earth Science–Journal of China University of Geosciences* **31**, 57–65 (in Chinese with English abstract).
- Zhang HF, Zhang BR, Harris N, Zhang L, Chen YL, Chen NS and Zhao ZD (2006b) U–Pb zircon SHRIMP ages, geochemical and Sr–Nd–Pb isotopic compositions of intrusive rocks from the Longshan–Tianshui area in the southeast corner of the Qilian orogenic belt, China: constraints on petrogenesis and tectonic affinity. *Journal of Asian Earth Sciences* **27**, 751–64.
- Zhang J, Long XP, Dong YP, Li J, Gao YL and Zhao BS (2019) Petrogenesis, tectonic setting and formation age of the metaperidotites in the Lajishan ophiolite, Central Qilian Block, NW China. *Journal of Asian Earth Sciences* **186**, 104076.
- Zhang JX, Yu SY, Li YS, Yu XX, Lin YH and Mao XH (2015a) Subduction, accretion and closure of Proto-Tethyan Ocean: Early Paleozoic accretion/collision orogeny in the Altun–Qilian–North Qaidam orogenic system. *Acta Petrologica Sinica* **31**, 3531–54 (in Chinese with English abstract).
- Zhang LC, Zhou XH, Ying JF, Wang F, Guo F, Wan B and Chen ZG (2008) Geochemistry and Sr–Nd–Pb–Hf isotopes of early Cretaceous basalts from the Great Xing’an Range, NE China: implications for their origin and mantle source characteristics. *Chemical Geology* **256**, 12–23.
- Zhang LQ, Zhang HF, Zhang SS, Xiong ZL, Luo BJ, Yang H, Pan FB, Zhou XC, Xu WC and Guo L (2017a) Lithospheric delamination in post-collisional setting: evidence from intrusive magmatism from the North Qilian orogen to southern margin of the Alxa block, NW China. *Lithos* **288–289**, 20–34.
- Zhang YQ, Song SG, Yang LM, Su L, Niu YL, Allen MB and Xu X (2017b) Basalts and picrites from a plume-type ophiolite in the South Qilian Accretionary Belt, Qilian Orogen: accretion of a Cambrian Oceanic Plateau? *Lithos* **278–281**, 97–110.
- Zhang ZW, Li WY, Wang YL and Gao YB (2015b) The genesis study on Xiaoshentang basic-ultrabasic intrusion associated with Ni–Cu mineralization in Hualong, southern Qilian Mountains: zircon geochronology, geochemistry and Sr–Nd isotopic constraints. *Acta Petrologica Sinica* **31**, 2539–48 (in Chinese with English abstract).
- Zuza AV, Wu C, Reith RC, Yin A, Li JH, Zhang JY, Zhang YX, Wu L and Liu WC (2018) Tectonic evolution of the Qilian Shan: an early Paleozoic orogeny reactivated in the Cenozoic. *Geological Society of America Bulletin* **130**, 881–925.